

An Elementarily Simple Galerkin Meshless Method: the Fragile Points Method (FPM) Using Point Stiffness Matrices, for 2D Elasticity Problems in Complex Domains

Tian Yang¹, Leiting Dong^{2,*}, Satya N. Atluri³

¹Graduate student, School of Aeronautic Science and Engineering, Beihang University, China

²Professor, School of Aeronautic Science and Engineering, Beihang University, China

³Presidential Chair & University Distinguished Professor of Texas Tech University, USA

SUMMARY

The Fragile Points Method (FPM) is a stable and elementarily simple, meshless Galerkin weak-form method, employing simple, local, polynomial, Point-based, discontinuous and identical trial and test functions which are derived from the Generalized Finite Difference method. Numerical Flux Corrections are introduced in the FPM to resolve the inconsistency caused by the discontinuous trial functions. Given the simple polynomial characteristic of trial and test functions, integrals in the Galerkin weak form can be calculated in the FPM without much effort. With the global matrix being sparse, symmetric and positive definitive, the FPM is suitable for large-scale simulations. Additionally, because of the inherent discontinuity of trial and test functions, we can easily cut off the interaction between Points and introduce cracks, rupture, fragmentation based on physical criteria. In this paper, we have studied the applications of the FPM to linear elastic mechanics and several numerical examples of 2D linear elasticity are computed. The results suggest the FPM is accurate, robust, consistent and convergent. Volume locking does not occur in the FPM for nearly incompressible materials. Besides, a new, simple and efficient approach to tackle pre-existing cracks in the FPM is also illustrated in this paper and applied to mode-I crack

* Corresponding author. Email address: ltdong@buaa.edu.cn (L. Dong).

problems.

KEY WORDS: Solids; Elasticity; Meshfree methods; Fragile Points Method; Numerical Flux Corrections; Mode-I crack

1. INTRODUCTION

Structural stress analysis is crucial and necessary in diverse engineering fields, such as aeronautics, astronautics, automobile engineering, etc. From the design, manufacture to maintenance of products, structural stress analysis plays a crucial role. Because of its significance, numerous researchers have been focusing on improving the accuracy and efficiency of this procedure for decades.

The Finite Element Method (FEM) is mature, reliable and widely used in structural stress analysis [1]. This method employs contiguous elements, and Element-based, local, polynomial, interelement-continuous trial and test functions. Because the trial and test functions are Element-based, the Galerkin weak form leads to Element Stiffness Matrices. Therefore, integrals in the Galerkin weak form underlying the FEM are easy to compute. The symmetry and sparsity of the global stiffness matrix make the FEM suitable and efficient in large-scale simulations. However, the accuracy of the FEM greatly depends on the quality of mesh. In order to obtain satisfactory solutions, many efforts are usually spent on meshing. Especially, even if simulations are initialized with a high-quality mesh structure, mesh distortion will occur in the case of large deformations and the precision of solutions decreases dramatically. In order to study the formation of cracks, rupture and fragmentation, methods such as remeshing, deleting elements, and Cohesive-Zone models are often used.

Meshless methods, which eliminate mesh structure partly or completely, have been invented and developed since the end of last century. Element Free Galerkin (EFG) [2] and Meshless Local Petrov-Galerkin (MLPG) [3] methods are two classical meshless weak-form methods based on the “Global Galerkin” and “Local Petrov-Galerkin” weak forms, respectively. While the EFG uses the same Node-based trial and test functions, the MLPG method uses different trial and test function spaces. The test function can be Dirac function or Heaviside function. These two meshless methods have mainly utilized

Moving Least Squares (MLS) or Radial Basis Function (RBF) approximations to deduce Node-based trial functions. With MLS and RBF approximations, higher-order continuity is easy to achieve. Besides, since individual nodes have replaced mesh structure, EFG and MLPG can conveniently insert or remove additional nodes and bypass the influence of distortion even in large deformation and fracture cases (e.g. [4], [5]). However, on the other hand, the trial functions obtained by the MLS or RBF method are rational functions and grossly complex. Therefore, the computation of integrals in the weak forms in either EFG or MLPG is extremely tedious, less accurate and even can influence the method's stability. To reduce the computational cost and improve the accuracy of integration, some special, new types of numerical integration methods, for example, the series of nodal integration methods [6], are often adopted.

Smoothed Particle Hydrodynamics (SPH) method [7], as a kind of meshless particle method, is simpler in form and needs less computational cost. Nevertheless, the SPH approach is based on a strong form, instead of a weak form. Demonstrating this method's stability is not an easy task. Besides, tensile instability will occur in the SPH, if we use Smoothed Kernel functions to calculate derivatives.

Peridynamics [8], as a relatively new method, is based on a different set of theories rather than the traditional continuum mechanics. Therefore, those classical constitutive models and engineering experience which scientists and engineers have developed for decades are difficult to be applied exactly and directly in Peridynamics, which is still far from being applicable to large-scale practical engineering situations.

From the above discussion, we can conclude that simple, local, polynomial, "Point-Based" shape functions are helpful in the calculation of integrals in the weak form. Besides, a weak-form method can have a better performance on stability. But with these requirements, it is difficult to keep the trial and test functions continuous over the entire domain. In our previous paper, we have developed the Fragile Points Method [9] for the first time. The FPM approach employs very simple, local, polynomial, Point-based and discontinuous shape functions constructed by the Generalized Finite Difference method. Since the FPM uses "Point-Based" trial and test functions in a Galerkin weak form, the method leads to "Point Stiffness Matrices" as opposed to the Element

Stiffness Matrices in the FEM. Numerical Flux Corrections are introduced in the FPM to solve the inconsistency caused by the method's discontinuity of trial and test functions. Integrals in the Galerkin weak form can be computed easily with Gauss Integration method or just analytically. Like the FEM, since the FPM is based on a Galerkin weak form, a symmetric, sparse and positive definitive global matrix can be deduced in the FPM, which means the FPM can be easily used in large-scale simulations. More importantly, because of the discontinuity of functions, we can easily cut off the interaction between two Points and introduce cracks, rupture or fragmentation without much effort.

In this paper, we formulate and apply the FPM for solving linear elasticity problems on complex shaped domains. A new, simple and efficient approach to introduce cracks in the FPM is also illustrated in this paper. The procedure for constructing Point-based trial and test functions is introduced in Section 2. The Interior Penalty Numerical Fluxes and the numerical implementation of the FPM for elasticity are discussed in Section 3. In Section 4, several numerical examples for 2D linear elasticity problems are studied and specific steps to deal with cracks in the FPM are introduced. Last, a conclusion and some discussions for further studies on modeling the formation of cracks, rupture and fragmentation are given in Section 5.

2. LOCAL, POLYNOMIAL, POINT-BASED, DISCONTINUOUS TRIAL AND TEST FUNCTIONS

For the linear elasticity, the governing equations are given in Eq. (2.1),

$$\begin{cases} \varepsilon_{ij}(u) = \frac{1}{2}(u_{i,j} + u_{j,i}) \\ \sigma_{ij,j}(u) + f_i = 0 \\ \sigma_{ij}(u) = D_{ijkl}\varepsilon_{kl}(u) \end{cases} \quad \text{in } \Omega \quad (2.1)$$

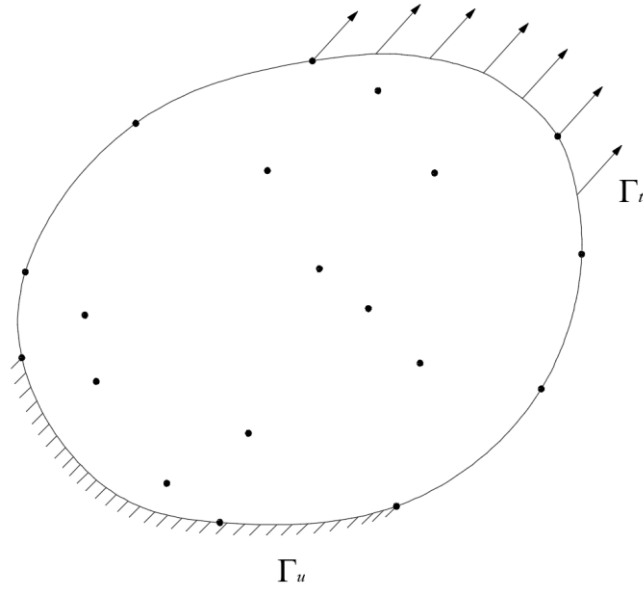
where Ω is the problem domain; σ_{ij} , ε_{ij} and u_i stand for the stress tensor, strain tensor and displacement vector, respectively; f_i is the body force and D_{ijkl} connotes

the fourth order linear elasticity tensor.

The corresponding boundary conditions are shown in Eq. (2.2), where Γ_u and Γ_t are displacement prescribed and traction prescribed boundaries, respectively; \bar{u}_i and \bar{t}_i denote the prescribed displacements and tractions on the corresponding boundaries, respectively; n_j stands for the unit vector outward to the external boundary $\partial\Omega$.

$$\begin{cases} u_i = \bar{u}_i & \text{on } \Gamma_u \\ \sigma_{ij}(u)n_j = \bar{t}_i & \text{on } \Gamma_t \end{cases} \quad (2.2)$$

Considering the problem domain Ω , as shown in Figure 1(a), several Points are distributed randomly inside the domain or on its boundary. Utilizing these Points, the domain can be partitioned into conforming and nonoverlapping subdomains of arbitrary shape, with only *one Point involved in each subdomain* (shown in Figure 1(b)). Numerous methods can be used for this partition, and in this paper, the Voronoi Diagram method is chosen. Thus, in the present Fragile Points Method, the construction of trial and test function is totally based on these randomly distributed Points. It should be noted that in contrast, in the FEM, the trial and test functions are Element-based and are continuous between Elements which are contiguous.



(a)

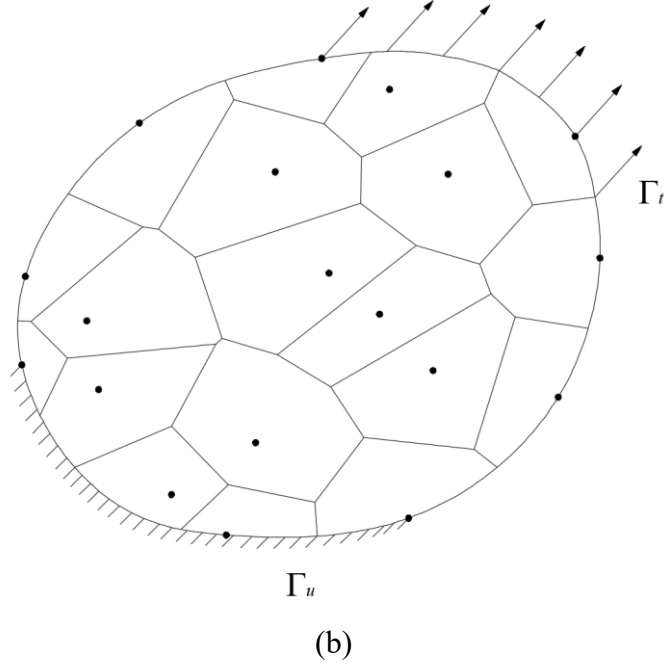


Figure 1 (a)(b). The problem domain and its partition

In each subdomain, we define the simple, local, polynomial, discontinuous displacement vector or trial function \mathbf{u}^h with the values of u_x , u_y (displacements in x and y directions, respectively) and their derivatives in x and y directions *at the internal Point*. For instance, the 2D linear displacement vector in the subdomain E_0 which contains the Point P_0 is given in Eq. (2.3),

$$\mathbf{u}^h(x, y) = \begin{bmatrix} u_x^h \\ u_y^h \end{bmatrix} = \begin{bmatrix} u_x^0 + \frac{\partial u_x}{\partial x} \Big|_{P_0} (x - x_0) + \frac{\partial u_x}{\partial y} \Big|_{P_0} (y - y_0) \\ u_y^0 + \frac{\partial u_y}{\partial x} \Big|_{P_0} (x - x_0) + \frac{\partial u_y}{\partial y} \Big|_{P_0} (y - y_0) \end{bmatrix} \quad (x, y) \in E_0 \quad (2.3)$$

where (x_0, y_0) are the coordinates of the Point P_0 ; $\begin{bmatrix} u_x^0 & u_y^0 \end{bmatrix}^T$ is the value of \mathbf{u}^h at P_0 ; Derivatives $\begin{bmatrix} \frac{\partial u_x}{\partial x} & \frac{\partial u_x}{\partial y} & \frac{\partial u_y}{\partial x} & \frac{\partial u_y}{\partial y} \end{bmatrix}^T \Big|_{P_0}$ are the yet unknown coefficients.

It is a crucial step to determine the derivatives $\begin{bmatrix} \frac{\partial u_x}{\partial x} & \frac{\partial u_x}{\partial y} & \frac{\partial u_y}{\partial x} & \frac{\partial u_y}{\partial y} \end{bmatrix}^T \Big|_{P_0}$. In our

work, we have used the Generalized Finite Difference (GFD) method [10] to calculate the derivatives at each Point.

The first step for the GFD method is to define the support of the Point P_0 . Usually, we prefer to define the support by drawing a circle at P_0 and assume all the Points included in that circle have interaction with P_0 (shown in Figure 2(a)). Alternatively, we can replace the circular support with a square one or other shapes. In this paper, the support of P_0 is defined to contain all its nearest neighboring points in the Voronoi Diagram partition (shown in Figure 2(b)). These neighboring points are named as P_1, P_2, \dots, P_m .

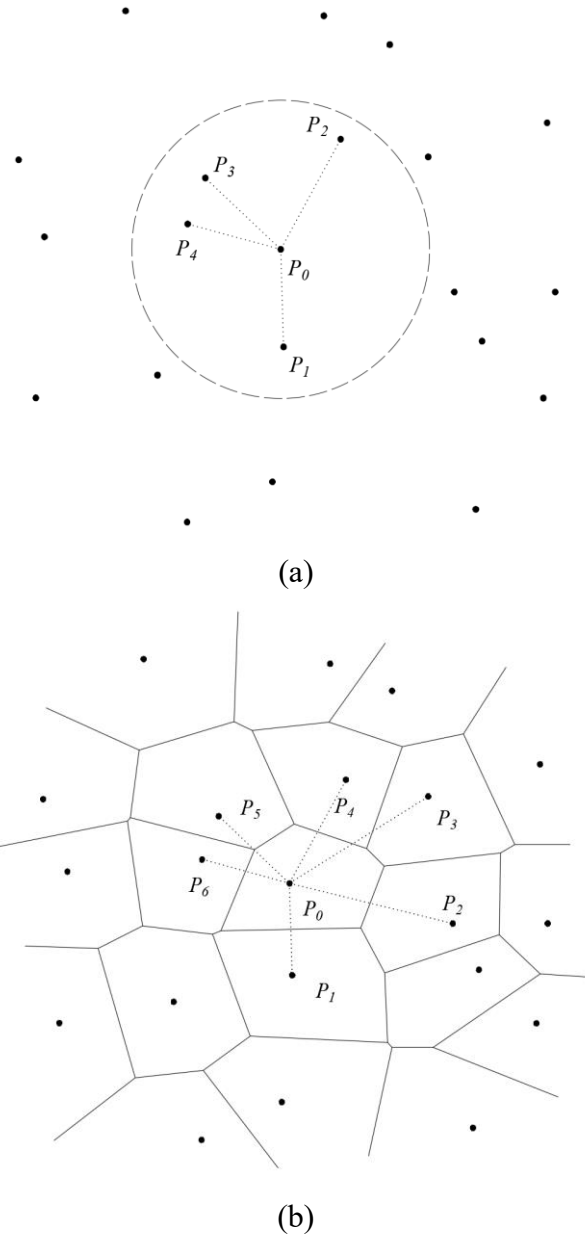


Figure 2(a) (b). Two kinds of support of P_0

After defining the support of P_0 , we define a weighted discrete L^2 norm J in a matrix form,

$$J = (\mathbf{A}\mathbf{a} + \mathbf{u}_0 - \mathbf{u}_m)^T \mathbf{W} (\mathbf{A}\mathbf{a} + \mathbf{u}_0 - \mathbf{u}_m) \quad (2.4)$$

where

$$\mathbf{A} = \begin{bmatrix} x_1 - x_0 & y_1 - y_0 & 0 & 0 \\ 0 & 0 & x_1 - x_0 & y_1 - y_0 \\ x_2 - x_0 & y_2 - y_0 & 0 & 0 \\ 0 & 0 & x_2 - x_0 & y_2 - y_0 \\ \vdots & \vdots & \vdots & \vdots \\ x_m - x_0 & y_m - y_0 & 0 & 0 \\ 0 & 0 & x_m - x_0 & y_m - y_0 \end{bmatrix}$$

$$\mathbf{a} = \left[\frac{\partial u_x}{\partial x} \quad \frac{\partial u_x}{\partial y} \quad \frac{\partial u_y}{\partial x} \quad \frac{\partial u_y}{\partial y} \right]^T \bigg|_{P_0}$$

$$\mathbf{u}_0 = \left(\begin{bmatrix} u_x^0 & u_y^0 & u_x^0 & u_y^0 & \cdots & u_x^0 & u_y^0 \end{bmatrix}_{1 \times 2m} \right)^T$$

$$\mathbf{u}_m = \begin{bmatrix} u_x^1 & u_y^1 & u_x^2 & u_y^2 & \cdots & u_x^m & u_y^m \end{bmatrix}^T$$

$$\mathbf{W} = \begin{bmatrix} w_x^1 & 0 & 0 & \cdots & 0 \\ 0 & w_y^1 & \ddots & \ddots & \vdots \\ 0 & \ddots & \ddots & \ddots & 0 \\ \vdots & \ddots & \ddots & w_x^m & 0 \\ 0 & \cdots & 0 & 0 & w_y^m \end{bmatrix}$$

(x_i, y_i) are the coordinates of P_i ; $\begin{bmatrix} u_x^i & u_y^i \end{bmatrix}^T$ is the value of \mathbf{u}^h at P_i ; $\begin{bmatrix} w_x^i & w_y^i \end{bmatrix}^T$ is the value of the weight function at P_i ($i=1,2,3,\dots,m$). For convenience, weight functions are taken to be constants in this paper.

By solving the stationarity of J in Eq. (2.4), we can derive the derivative vector \mathbf{a} at P_0 .

$$\mathbf{a} = (\mathbf{A}^T \mathbf{W} \mathbf{A})^{-1} \mathbf{A}^T \mathbf{W} (\mathbf{u}_m - \mathbf{u}_0) \quad (2.5)$$

Besides, $\mathbf{u}_m - \mathbf{u}_0$ can be transformed into the following form,

$$(\mathbf{u}_m - \mathbf{u}_0) = [\mathbf{I}_1 \quad \mathbf{I}_2] \mathbf{u}_E \quad (2.6)$$

where

$$\mathbf{u}_E = [u_x^0 \quad u_y^0 \quad u_x^1 \quad u_y^1 \quad \cdots \quad u_x^m \quad u_y^m]^T$$

$$\mathbf{I}_1 = \begin{bmatrix} -1 & 0 \\ 0 & -1 \\ -1 & 0 \\ 0 & -1 \\ \vdots & \vdots \\ -1 & 0 \\ 0 & -1 \end{bmatrix}_{2m \times 2} \quad \mathbf{I}_2 = \begin{bmatrix} 1 & 0 & \cdots & 0 \\ 0 & 1 & \ddots & \vdots \\ \vdots & \ddots & \ddots & 0 \\ 0 & \cdots & 0 & 1 \end{bmatrix}_{2m \times 2m}$$

Substituting Eq. (2.6) into Eq. (2.5), we obtain the relationship between \mathbf{a} and \mathbf{u}_E .

$$\mathbf{a} = \mathbf{C} \mathbf{u}_E \quad (2.7)$$

where

$$\mathbf{C} = (\mathbf{A}^T \mathbf{W} \mathbf{A})^{-1} \mathbf{A}^T \mathbf{W} [\mathbf{I}_1 \quad \mathbf{I}_2]$$

Finally, by substituting Eq. (2.7) into Eq. (2.3), the relationship between \mathbf{u}^h and \mathbf{u}_E

is obtained in Eq. (2.8), where the matrix \mathbf{N} is called the shape function of \mathbf{u}^h in E_0 .

$$\mathbf{u}^h = \mathbf{N} \mathbf{u}_E \quad (2.8)$$

$$\mathbf{N} = \begin{bmatrix} x - x_0 & y - y_0 & 0 & 0 \\ 0 & 0 & x - x_0 & y - y_0 \end{bmatrix} \mathbf{C} + \mathbf{I}_3$$

$$= \begin{bmatrix} N_0 & 0 & N_1 & 0 & \cdots & N_m & 0 \\ 0 & N_0 & 0 & N_1 & \cdots & 0 & N_m \end{bmatrix}_{2 \times (2m+2)}$$

$$\text{where } \mathbf{I}_3 = \begin{bmatrix} 1 & 0 & 0 & \cdots & 0 \\ 0 & 1 & 0 & \cdots & 0 \end{bmatrix}_{2 \times (2m+2)}$$

According to the Eq. (2.1), the corresponding strain vector $\boldsymbol{\varepsilon}^h$ and stress vector $\boldsymbol{\sigma}^h$ in terms of \mathbf{u}_E are given in Eq. (2.9),

$$\begin{aligned}
\boldsymbol{\varepsilon}^h = \begin{bmatrix} \varepsilon_x^h \\ \varepsilon_y^h \\ \gamma_{xy}^h \end{bmatrix} &= \begin{bmatrix} \frac{\partial}{\partial x} & 0 \\ 0 & \frac{\partial}{\partial y} \\ \frac{\partial}{\partial y} & \frac{\partial}{\partial x} \end{bmatrix} \mathbf{u}^h = \begin{bmatrix} 1 & 0 & 0 & 0 \\ 0 & 0 & 0 & 1 \\ 0 & 1 & 1 & 0 \end{bmatrix} \mathbf{C} \mathbf{u}_E = \mathbf{B} \mathbf{u}_E \\
\boldsymbol{\sigma}^h = \begin{bmatrix} \sigma_x^h \\ \sigma_y^h \\ \tau_{xy}^h \end{bmatrix} &= \mathbf{D} \begin{bmatrix} \varepsilon_x \\ \varepsilon_y \\ \gamma_{xy} \end{bmatrix} = \mathbf{D} \mathbf{B} \mathbf{u}_E
\end{aligned} \tag{2.9}$$

where \mathbf{D} is the stress-strain matrix. In this paper we consider the material to be isotropic for simplicity.

$$\begin{aligned}
\mathbf{D} &= \frac{\bar{E}}{1-\bar{\nu}^2} \begin{bmatrix} 1 & \bar{\nu} & 0 \\ \bar{\nu} & 1 & 0 \\ 0 & 0 & (1-\bar{\nu})/2 \end{bmatrix} \\
\text{with } \bar{E} &= \begin{cases} E & (\text{for plane stress}) \\ \frac{E}{1-\nu^2} & (\text{for plane strain}) \end{cases} \\
\bar{\nu} &= \begin{cases} \nu & (\text{for plane stress}) \\ \frac{\nu}{1-\nu} & (\text{for plane strain}) \end{cases}
\end{aligned}$$

Following the same procedure, we can derive \mathbf{u}^h in each subdomain $E_i \in \Omega$.

Eventually, the displacement vector \mathbf{u}^h in the entire domain can be obtained. The corresponding test function \mathbf{v} is prescribed to possess the same shape as the trial function in each subdomain, in the present FPM based on the Galerkin weak form.

Reviewing the process of constructing trial and test functions, we can see that no continuity requirement exists on the internal boundary between two neighboring subdomains. In other words, these two subdomains have their own function values on their common boundary. Therefore, only simple, local, polynomial, Point-based and piecewise-continuous trial and test functions are obtained in the problem domain Ω .

To illustrate the discontinuity of trial functions and shape functions, a 2D example is shown here. We assume that 25 Points are scattered irregularly in a 1×1 square. The graphical representation of all the shape functions about Point 13 (the subscripts in Eq.

(2.8) equal 13) is given in Figure 3. The corresponding trial function of u_x simulating the exponential function $e^{-10(x-0.5)^2-10(y-0.5)^2}$ is shown in Figure 4.

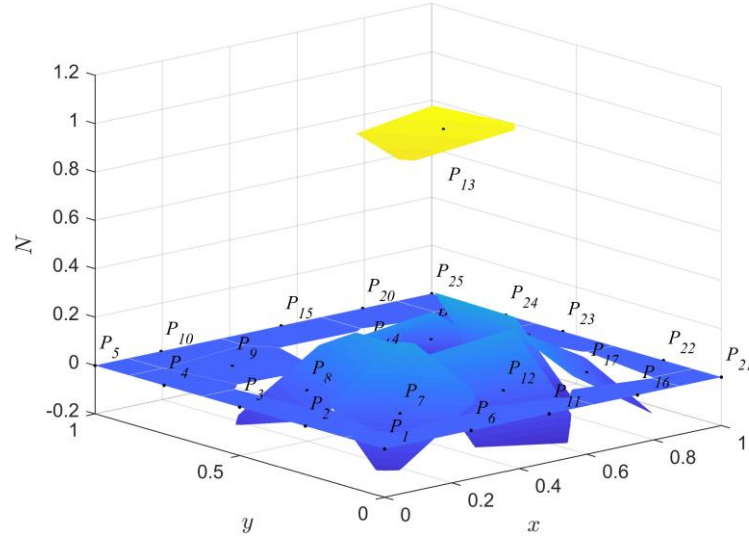


Figure 3. The shape functions about Point 13

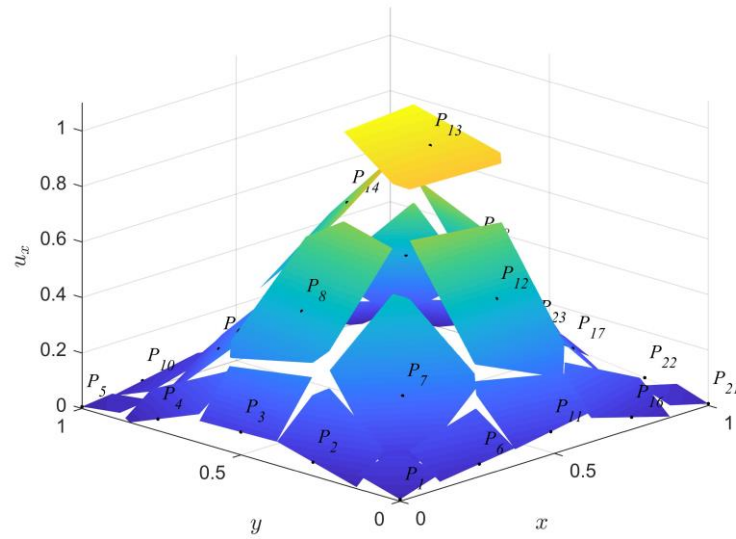


Figure 4. The trial function simulating an exponential function

Unfortunately, because of this discontinuity of trial and test functions, if we directly use the trial and test functions in the traditional Galerkin weak form which is widely used in the FEM, EFG and other numerical methods, the solution will be inconsistent, inaccurate and cannot pass the patch tests [9]. In order to solve this inconsistency problem, Numerical Flux Corrections have been introduced to the FPM.

3. NUMERICAL FLUX CORRECTIONS AND NUMERICAL IMPLEMENTATION

3.1 Interior Penalty (IP) Numerical Flux Corrections for elasticity problems

Numerical Fluxes, frequently used in Discontinuous Galerkin Methods, are employed in the FPM to resolve the inconsistency caused by the discontinuity of trial and test functions. A variety of Numerical Fluxes have been developed and studied by various researchers. These Numerical Fluxes have different effects on accuracy, stability and computational cost of a method. In our work, we prefer the Interior Penalty Numerical Fluxes which can lead to consistent and stable results and symmetric global stiffness matrices.

The governing equations of linear elasticity in 2D have been shown in Eq. (2.1). We multiply the second equation by the test function \mathbf{v} then integrate it on the subdomain E by parts,

$$\int_E \sigma_{ij}(u) v_{i,j} d\Omega - \int_{\partial E} \sigma_{ij}(u) n_j v_i d\Gamma = \int_E f_i v_i d\Omega \quad (3.1)$$

where ∂E is the boundary of the subdomain E , \mathbf{n} is the unit vector outward to ∂E .

For every subdomain $E_i \in \Omega$, Eq. (3.1) should be satisfied. Therefore, we sum Eq. (3.1) over all subdomains.

$$\sum_{E \in \Omega} \int_E \sigma_{ij}(u) v_{i,j} d\Omega - \sum_{E \in \Omega} \int_{\partial E} \sigma_{ij}(u) n_j v_i d\Gamma = \sum_{E \in \Omega} \int_E f_i v_i d\Omega \quad (3.2)$$

Considering the symmetry of stress tensor ($\sigma_{ij} = \sigma_{ji}$), we can transform the first term of Eq. (3.2) into the following form,

$$\sum_{E \in \Omega} \int_E \sigma_{ij}(u) v_{i,j} d\Omega = \sum_{E \in \Omega} \int_E \sigma_{ij}(u) \epsilon_{ij}(v) d\Omega \quad (3.3)$$

Let Γ denote the set of all external and internal boundaries and $\Gamma_h = \Gamma - \Gamma_t - \Gamma_u$ stands for the set of all internal boundaries. For the convenience, we rewrite the second term in Eq. (3.2) with the jump operator $[\cdot]$ and average operator $\{\cdot\}$.

$$\begin{aligned} \sum_{E \in \Omega} \int_{\partial E} \sigma_{ij}(u) n_j v_i d\Gamma &= \sum_{e \in \Gamma_h} \int_e \left([\sigma_{ij}(u) n_j^e] \{v_i\} + \{\sigma_{ij}(u) n_j^e\} [v_i] \right) d\Gamma \\ &+ \sum_{e \in \Gamma_u} \int_e \{\sigma_{ij}(u) n_j^e\} [v_i] d\Gamma + \sum_{e \in \Gamma_t} \int_e \{\sigma_{ij}(u) n_j^e\} [v_i] d\Gamma \end{aligned} \quad (3.4)$$

When $e \in \Gamma_h$ (assuming e is shared by subdomains E_1 and E_2), n_j^e is a unit vector normal to e and points from E_1 to E_2 . The average $\{\}$ and jump $[\]$ operator for any quantity w , at an internal boundary are defined as Eq. (3.5).

$$\begin{aligned} [w] &= w|_e^{E_1} - w|_e^{E_2} \\ \{w\} &= \frac{1}{2} \left(w|_e^{E_1} + w|_e^{E_2} \right) \end{aligned} \quad (3.5)$$

When $e \in \partial\Omega$, n_j^e is outward to $\partial\Omega$ and the average $\{\}$ and jump $[\]$ operator are defined as below.

$$\begin{aligned} [w] &= w|_e \\ \{w\} &= w|_e \end{aligned}$$

It should be noted that for two neighboring subdomains, no matter which one is chosen as E_1 , the value of Eq (3.4) stays the same. If $\sigma_{ij}(u)$ is the exact solution in an intact contiguous domain, there should be no jump on internal boundaries, in other words, $[\sigma_{ij}(u)n_j^e] = 0$, i.e., tractions are reciprocated at internal intact boundaries. Besides, with the traction boundary condition $\sigma_{ij}(u)n_j = \bar{t}_i$, Eq. (3.4) can be rewritten as below.

$$\sum_{E \in \Omega} \int_{\partial E} \sigma_{ij}(u) n_j v_i d\Gamma = \sum_{e \in \Gamma_h \cup \Gamma_u} \int_e \{\sigma_{ij}(u) n_j^e\} [v_i] d\Gamma + \sum_{e \in \Gamma_t} \int_e \bar{t}_i v_i d\Gamma \quad (3.6)$$

Eventually, we substitute Eq. (3.3), Eq. (3.6) into Eq. (3.2), and add two boundary integrals $-\sum_{e \in \Gamma_h \cup \Gamma_u} \int_e \{\sigma_{ij}(v) n_j^e\} [u_i] d\Gamma$ and $\sum_{e \in \Gamma_h \cup \Gamma_u} \frac{\eta}{h_e} \int_e [u_i] [v_i] d\Gamma$. Then we obtain the

FPM with Interior Penalty Numerical Flux Corrections for elasticity problems,

$$\begin{aligned} & \sum_{E \in \Omega} \int_E \sigma_{ij}(u) \varepsilon_{ij}(v) d\Omega - \sum_{e \in \Gamma_h \cup \Gamma_u} \int_e \{\sigma_{ij}(u) n_j^e\} [v_i] d\Gamma \\ & - \sum_{e \in \Gamma_h \cup \Gamma_u} \int_e \{\sigma_{ij}(v) n_j^e\} [u_i] d\Gamma + \sum_{e \in \Gamma_h \cup \Gamma_u} \frac{\eta}{h_e} \int_e [u_i] [v_i] d\Gamma \\ & = \sum_{E \in \Omega} \int_E f_i v_i d\Omega + \sum_{e \in \Gamma_t} \int_e \bar{t}_i v_i d\Gamma - \sum_{e \in \Gamma_u} \int_e \sigma_{ij}(v) n_j^e \bar{u}_i d\Gamma + \sum_{e \in \Gamma_u} \frac{\eta}{h_e} \int_e \bar{u}_i v_i d\Gamma \end{aligned} \quad (3.7)$$

where h_e is an edge-dependent parameter and equal to the length of the boundary in

this paper; η is a positive number independent of the edge size. It should be noted that with IP Numerical Flux Corrections, the method is only stable when the penalty parameter η is large enough [11]. A discussion about the effect of the penalty parameter is given in Section 4 and more information can be found in [12].

We can find that in Eq. (3.7), if the trial function and test function utilize the same shape functions, the FPM with IP Numerical Flux Corrections is a symmetric Galerkin weak-form approach. Moreover, displacement boundary conditions are imposed weakly in Eq. (3.7). If we impose $u_i = \bar{u}_i$ strongly at the boundary points, Eq. (3.7) can be simplified as follows.

$$\begin{aligned}
& \sum_{E \in \Omega} \int_E \sigma_{ij}(u) \varepsilon_{ij}(v) d\Omega - \sum_{e \in \Gamma_h} \int_e \{ \sigma_{ij}(u) n_j^e \} [v_i] d\Gamma \\
& - \sum_{e \in \Gamma_h} \int_e \{ \sigma_{ij}(v) n_j^e \} [u_i] d\Gamma + \sum_{e \in \Gamma_h} \frac{\eta}{h_e} \int_e [u_i] [v_i] d\Gamma \\
& = \sum_{E \in \Omega} \int_E f_i v_i d\Omega + \sum_{e \in \Gamma_t} \int_e \bar{t}_i v_i d\Gamma
\end{aligned} \tag{3.8}$$

For brevity, we can change Eq. (3.8) from a tensor form to a matrix form,

$$\begin{aligned}
& \sum_{E \in \Omega} \int_E \boldsymbol{\varepsilon}_v^T \boldsymbol{\sigma}_u d\Omega - \sum_{e \in \Gamma_h} \int_e [\mathbf{v}]^T \{ \mathbf{n}_e \boldsymbol{\sigma}_u \} d\Gamma \\
& - \sum_{e \in \Gamma_h} \int_e \{ \mathbf{n}_e \boldsymbol{\sigma}_v \}^T [\mathbf{u}] d\Gamma + \sum_{e \in \Gamma_h} \frac{\eta}{h_e} \int_e [\mathbf{v}]^T [\mathbf{u}] d\Gamma \\
& = \sum_{E \in \Omega} \int_E \mathbf{v}^T \mathbf{f} d\Omega + \sum_{e \in \Gamma_t} \int_e \mathbf{v}^T \bar{\mathbf{t}} d\Gamma
\end{aligned} \tag{3.9}$$

where

$$\begin{aligned}
\boldsymbol{\sigma} &= \begin{bmatrix} \sigma_x \\ \sigma_y \\ \tau_{xy} \end{bmatrix} & \boldsymbol{\varepsilon} &= \begin{bmatrix} \varepsilon_x \\ \varepsilon_y \\ \gamma_{xy} \end{bmatrix} & \mathbf{u} &= \begin{bmatrix} u_x \\ u_y \end{bmatrix} & \mathbf{v} &= \begin{bmatrix} v_x \\ v_y \end{bmatrix} \\
\mathbf{n}_e &= \begin{bmatrix} n_x^e & 0 & n_y^e \\ 0 & n_y^e & n_x^e \end{bmatrix} & \mathbf{f} &= \begin{bmatrix} f_x \\ f_y \end{bmatrix} & \bar{\mathbf{t}} &= \begin{bmatrix} \bar{t}_x \\ \bar{t}_y \end{bmatrix}
\end{aligned}$$

Compared with the traditional Galerkin weak form [1], the Eq. (3.9) involves 3 extra boundary integrals on the left side, while the others stay identical. These additional boundary integrals are the contributions of the Interior Penalty Numerical Flux Corrections. To make the work clearer, if we define $\mathbf{v} = \delta \mathbf{u}$, the integrals on a specific

internal boundary (shown in Figure 5) are given in Eq. (3.10).

$$\begin{aligned}
& \int_e \frac{\eta}{h_e} \mathbf{v}^T \mathbf{u} - \{\mathbf{n}_e \boldsymbol{\sigma}_v\}^T [\mathbf{u}] - [\mathbf{v}]^T \{\mathbf{n}_e \boldsymbol{\sigma}_u\} d\Gamma \\
& = \delta \left\langle \int_e \frac{1}{2} \frac{\eta}{h_e} [\mathbf{u}]^T [\mathbf{u}] - \{\mathbf{n}_e \boldsymbol{\sigma}_u\}^T [\mathbf{u}] d\Gamma \right\rangle \\
& = \delta \langle \text{Bonding Energy} \rangle
\end{aligned} \tag{3.10}$$

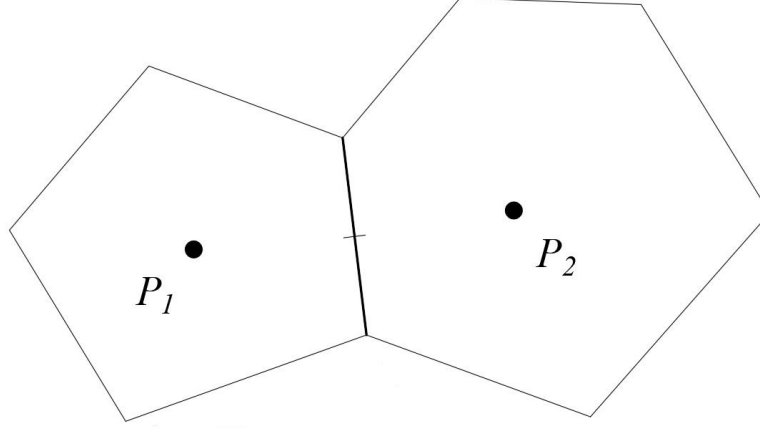


Figure 5. The integrals on a specific internal boundary

In a physical view, $\sum_{e \in \Gamma_h} \int_e \{\sigma_{ij}(u) n_j^e\} [v_i] d\Gamma$ and $\sum_{e \in \Gamma_h} \int_e \{\sigma_{ij}(v) n_j^e\} [u_i] d\Gamma$ are the extra virtual work caused by the discontinuity of displacements and non-reciprocity of tractions on internal boundaries, and $\sum_{e \in \Gamma_h} \frac{\eta}{h_e} \int_e [u_i] [v_i] d\Gamma$ play a role in restricting the jump of displacements as a kind of penalty functions. By postulating the physical quantities of energy required for the formation of cracks, rupture and fragmentation of unit length, criteria can be developed for rupture and fragmentation when these physical quantities exceed these bonding energies, by breaking the bonds between neighboring Points. Alternatively, one could postulate criteria for rupture between two subdomains, based on the discontinuity of the Eshelby tractions [13] between the two segments. Hence the present method is named the Fragile Points Method (FPM).

3.2 Numerical implementation

This section will concentrate on the numerical implementation of the FPM. The FPM with IP Numerical Flux Corrections can be written finally in the following matrix form,

$$\mathbf{K}\mathbf{q} = \mathbf{Q}$$

where \mathbf{K} is the global stiffness matrix, \mathbf{q} is the vector with nodal DOFs, \mathbf{Q} is the load vector.

In Section 2, we have obtained the shape function \mathbf{N} for \mathbf{u}^h and \mathbf{v} , \mathbf{B} for $\boldsymbol{\varepsilon}$, \mathbf{DB} for $\boldsymbol{\sigma}$. By substituting them into the first term of Eq. (3.9), we derive the Point Stiffness Matrix \mathbf{K}_E , which is defined as the contribution of each Point to the global stiffness matrix.

$$\mathbf{K}_E = \int_E \mathbf{B}^T \mathbf{DB} d\Omega \quad \text{where } E \in \Omega \quad (3.11)$$

For the boundary integrals, the corresponding boundary stiffness matrix \mathbf{K}_h is defined as below. The subscripts 1 and 2 denote which subdomain these shape functions belong to.

when $e \in \partial E_1 \cap \partial E_2$

$$\begin{aligned} \mathbf{K}_h = & -\frac{1}{2} \int_e \mathbf{N}_1^T \mathbf{n}_e \mathbf{DB}_1 d\Gamma - \frac{1}{2} \int_e \mathbf{B}_1^T \mathbf{Dn}_e^T \mathbf{N}_1 d\Gamma + \frac{\eta}{h_e} \int_e \mathbf{N}_1^T \mathbf{N}_1 d\Gamma \\ & - \frac{1}{2} \int_e \mathbf{N}_1^T \mathbf{n}_e \mathbf{DB}_2 d\Gamma + \frac{1}{2} \int_e \mathbf{B}_1^T \mathbf{Dn}_e^T \mathbf{N}_2 d\Gamma - \frac{\eta}{h_e} \int_e \mathbf{N}_1^T \mathbf{N}_2 d\Gamma \\ & + \frac{1}{2} \int_e \mathbf{N}_2^T \mathbf{n}_e \mathbf{DB}_1 d\Gamma - \frac{1}{2} \int_e \mathbf{B}_2^T \mathbf{Dn}_e^T \mathbf{N}_1 d\Gamma - \frac{\eta}{h_e} \int_e \mathbf{N}_2^T \mathbf{N}_1 d\Gamma \\ & + \frac{1}{2} \int_e \mathbf{N}_2^T \mathbf{n}_e \mathbf{DB}_2 d\Gamma + \frac{1}{2} \int_e \mathbf{B}_2^T \mathbf{Dn}_e^T \mathbf{N}_2 d\Gamma + \frac{\eta}{h_e} \int_e \mathbf{N}_2^T \mathbf{N}_2 d\Gamma \end{aligned} \quad (3.12)$$

In the FPM, the global stiffness matrix \mathbf{K} is obtained by assembling all the submatrices \mathbf{K}_E and \mathbf{K}_h . This assembling process is the same as what we do in the FEM. Eventually, the FPM will lead to a sparse, symmetric and positive definitive global stiffness matrix.

When linear interpolations are employed for \mathbf{u}^h , the shape function \mathbf{B} is constant and \mathbf{N} is linear in each subdomain. Therefore, the integral for submatrix \mathbf{K}_E can be calculated just multiplying the integrand by the area of the corresponding subdomain. For integrals on boundaries, the numerical integration and direct analytic computation are both effective. For Eq. (3.12), 2 Points Gauss integration can lead to exact solutions.

According to our results, reduced integration using only 1 Point can result in almost the same solutions as those obtained by 2 Points Gauss integration. In this paper, 1 Point Gauss integration method is used for boundary integrals.

4. NUMERICAL EXAMPLES

In this section, a variety of problems are solved with the FPM. In order to estimate the errors of numerical results conveniently, we define two relative errors r_u and r_E with the displacement L^2 norm and the energy norm, respectively.

$$\begin{aligned} r_u &= \frac{\|\mathbf{u}^h - \mathbf{u}^{\text{exact}}\|_{L^2}}{\|\mathbf{u}^{\text{exact}}\|_{L^2}} \\ r_E &= \frac{\|E^h - E^{\text{exact}}\|_E}{\|E^{\text{exact}}\|_E} \end{aligned} \quad (4.1)$$

$$\text{where } \|\mathbf{u}\|_{L^2} = \left(\int_{\Omega} \mathbf{u}^T \mathbf{u} d\Omega \right)^{1/2}, \quad \|E\|_E = \left(\frac{1}{2} \int_{\Omega} \boldsymbol{\varepsilon}^T \mathbf{D} \boldsymbol{\varepsilon} d\Omega \right)^{1/2}$$

4.1 Patch test

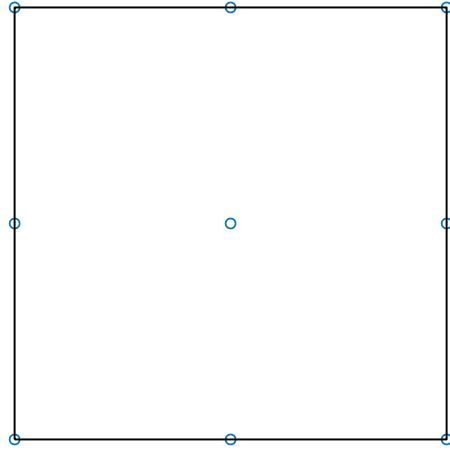
In this part, we design the following patch test in a unit square domain (shown in Figure 6) to examine the consistency of the FPM. Plane stress is considered, with the exact displacements and stresses prescribed as below

$$\begin{aligned} \mathbf{u} &= \begin{bmatrix} u_x \\ u_y \end{bmatrix} = \begin{bmatrix} x + y \\ x + y \end{bmatrix} \\ \boldsymbol{\sigma} &= \begin{bmatrix} \sigma_x \\ \sigma_y \\ \tau_{xy} \end{bmatrix} = \begin{bmatrix} \frac{E}{1-\nu} \\ \frac{E}{1-\nu} \\ \frac{E}{1+\nu} \end{bmatrix} \\ x, y &\in (0,1) \end{aligned} \quad (4.2)$$

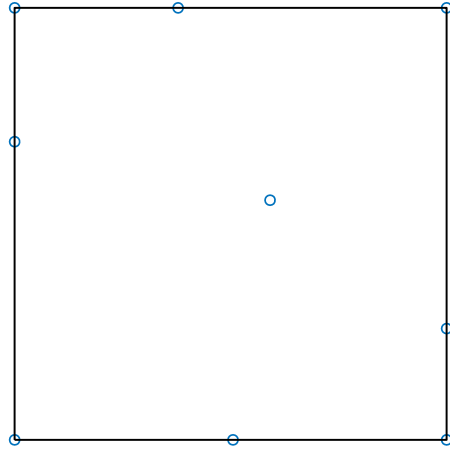
Displacement boundary conditions are imposed on the upper and bottom edges, and traction boundary conditions are prescribed on the left and right edges, according to Eq. (4.2). Since the solutions are linear for the displacements, when linear interpolations are employed for displacements, the numerical solutions \mathbf{u}^h and $\boldsymbol{\sigma}^h$

should be equal to those in Eq. (4.2).

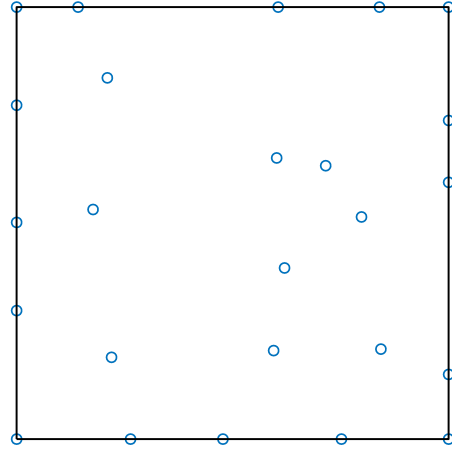
The distributions of points in 3 different patterns are given in Figure 6. In these three cases, no matter the points are scattered uniformly or randomly, the relative errors r_u and r_E are less than 5×10^{-7} with the penalty parameter $\eta \geq 1000E$ to restrict the jumps on internal boundaries. Therefore, we can conclude that the present FPM is consistent, and it is accurate enough to pass the patch tests.



(a) 9 regular points



(b) 9 irregular points



(c) 25 irregular points

Figure 6(a) (b) (c). Three distributions of Points for patch tests

4.2 Cantilever beam

In this section, we employ the FPM to solve a cantilever beam problem with a parabolic-shear load at one end (shown in Figure 7). The corresponding analytical solutions of displacements and stresses for the plane stress case are been given in [14].

$$\begin{aligned}
 u_x &= -\frac{P}{6EI} \left(y - \frac{H}{2} \right) \left[3x(2L-x) + (2+\nu)y(y-H) \right] \\
 u_y &= \frac{P}{6EI} \left[x^2(3L-x) + 3\nu(L-x) \left(y - \frac{H}{2} \right)^2 + \frac{4+5\nu}{4} H^2 x \right] \\
 \sigma_x &= -\frac{P}{I} (L-x) \left(y - \frac{H}{2} \right) \\
 \sigma_y &= 0 \\
 \tau_{xy} &= -\frac{Py}{2I} (y-H)
 \end{aligned} \tag{4.3}$$

where

$$I = \frac{H^3}{12}$$

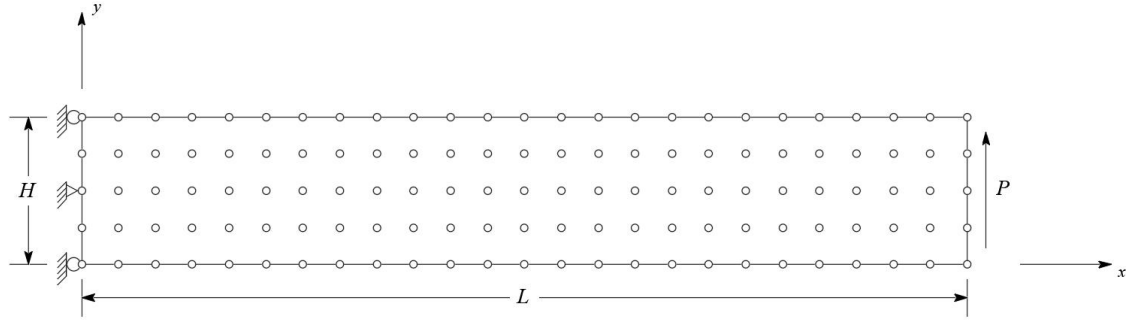
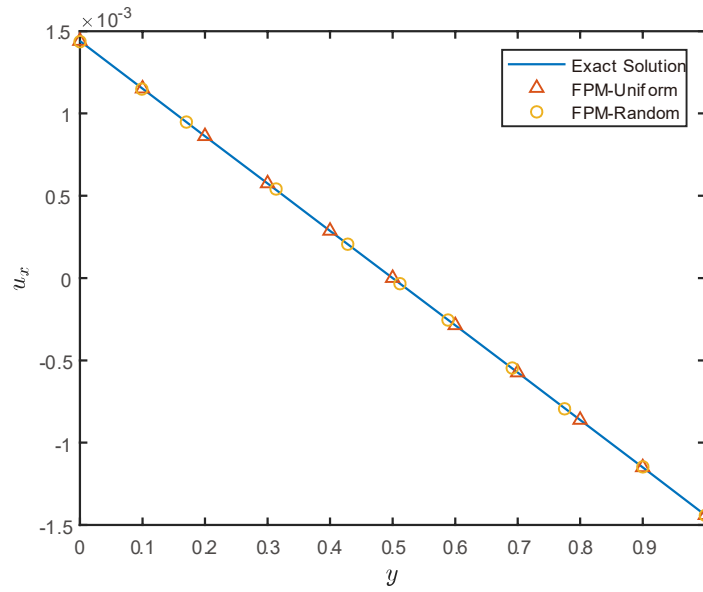


Figure 7. The cantilever beam with a parabolic-shear load

Specifically, we prescribe that $P = 1$, $E = 1 \times 10^5$, $H = 1$ and $L = 8$. Poisson's ratio ν is prescribed as 0.3 and the penalty parameter $\eta = E$. Displacement boundary conditions are imposed on the left and right edges of the beam, and traction boundary conditions are prescribed on the upper and bottom edges, according to Eq. (4.3). With 891 points distributed in the beam uniformly or randomly, the comparisons between numerical solutions u_x , σ_x and analytical solutions along the line $x = L/2$ are given in Figure 8(a) and (b), respectively.



(a)

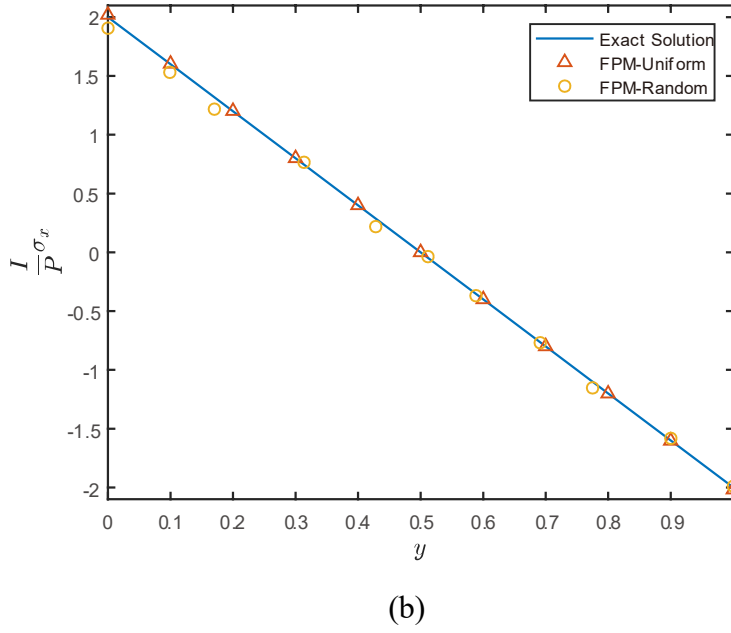


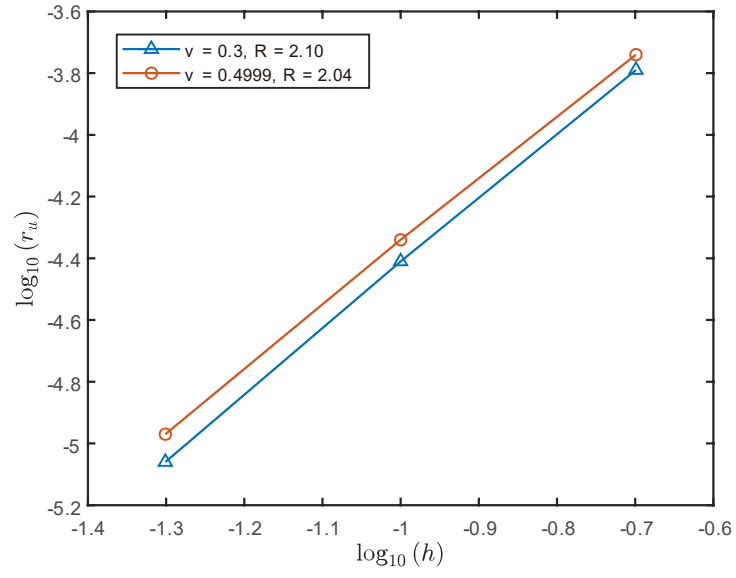
Figure 8(a). Numerical solutions of u_x along $x = L/2$

(b). Numerical solutions of σ_x along $x = L/2$

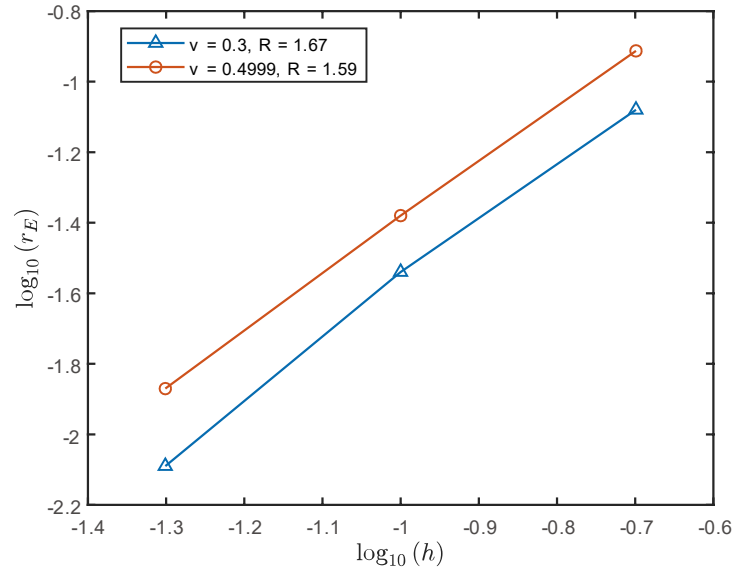
To demonstrate the convergence of the FPM, uniformly distributed 41×6 , 81×11 and 161×21 points are used to solve the problem respectively. Besides, the Poisson's ratio is set as 0.3 or 0.4999 to test whether the FPM can be used to model nearly incompressible materials.

The relations between h (the distance of two neighboring Points in x direction) and the relative errors r_u , r_E are shown in Figure 9(a) and (b), respectively. Also, the corresponding convergence rate R is given in Figure 9. Compared with the linear displacement-based FEM, whose convergence rates are 2 and 1 for displacements and the strain energy, respectively [1], the FPM shows a better performance in the convergence for the strain energy.

For the traditional FEM, when materials are nearly incompressible, volume locking leads to small solutions of the displacement fields. However, from Figure 9, it is obvious that the FPM performs well when $\nu = 0.4999$, which means that the FPM is a locking-free method for nearly incompressible materials.



(a)



(b)

Figure 9(a). Relative errors and convergence rates for r_u

(b). Relative errors and convergence rates for r_E

In Eq. (3.8), the accuracy and stability of the FPM is influenced by the penalty parameter η . Figure 10 is given to show the relation between relative errors and the penalty parameter. In this example, 161×21 points are distributed uniformly in the beam.

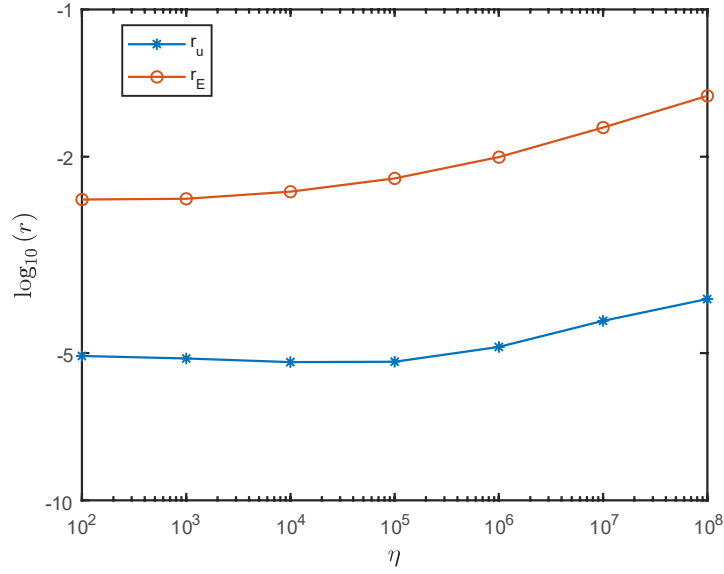
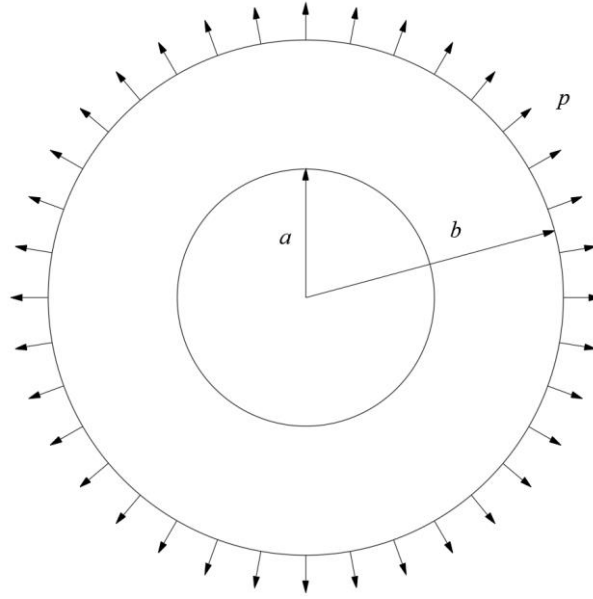


Figure 10. The relations between relative errors and η

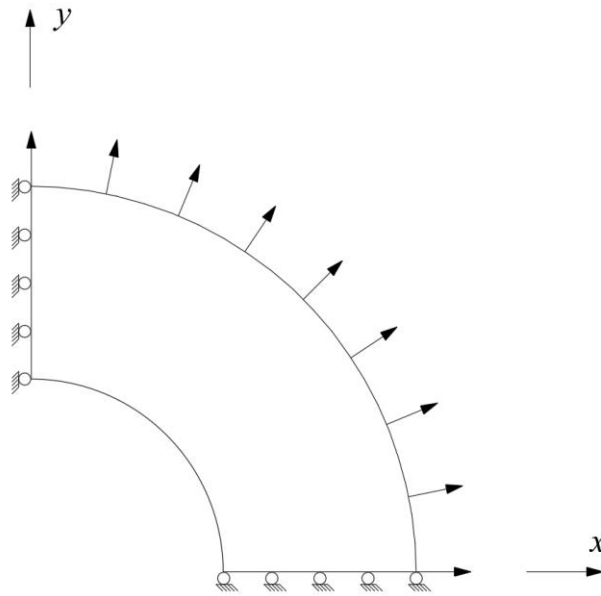
A larger penalty coefficient can result in smaller jumps of displacements on internal boundaries, but also will increase the condition number of the global matrix, thus affecting the precision of solutions [12]. From Figure 10, we can find that with the penalty parameter changing from a small value to a large one, the relative errors stay steady at first and then increase gradually. Based on the fact that the penalty parameter needs to be large enough to maintain the stability of the method [11], it is suggested to set it within the range from $10^{-1} \times E$ to $10^2 \times E$.

4.3 Ring with radial tensile traction

In this part, a ring with radial tensile traction is solved by the FPM (shown in Figure 11(a)). The ring is defined as $\{(x, y) | a^2 \leq x^2 + y^2 \leq b^2\}$ and it is subjected to a uniform radial tension. Since the ring is symmetric in geometry, we only model the upper right quarter (shown in Figure 11(b)). Symmetry boundary conditions are imposed on the left and bottom edges, which means $u_x = 0$, $t_y = 0$ for the left edge and $u_y = 0$, $t_x = 0$ for the bottom edge. Traction boundary conditions are imposed at $r = b$, according to the tensile traction p . The edge, $r = a$, is set to be a free boundary.



(a)



(b)

Figure 11(a). The ring with radial tension

(b). The ring on fourfold symmetry

Specifically, we prescribe that $a = 1$, $b = 2$ and $p = 1$ for the ring. The exact solutions for stresses and displacements are given in Eqs. (4.4) and (4.5), respectively, where (r, θ) are the polar coordinates and θ is anticlockwise measured from the positive x -axis. The problem is solved considering plane stress with $E = 1 \times 10^5$ and $\nu = 0.3$. The penalty parameter is set as $\eta = E$.

$$\sigma_r = \frac{b^2}{b^2 - a^2} \left(1 - \frac{a^2}{r^2} \right) p$$

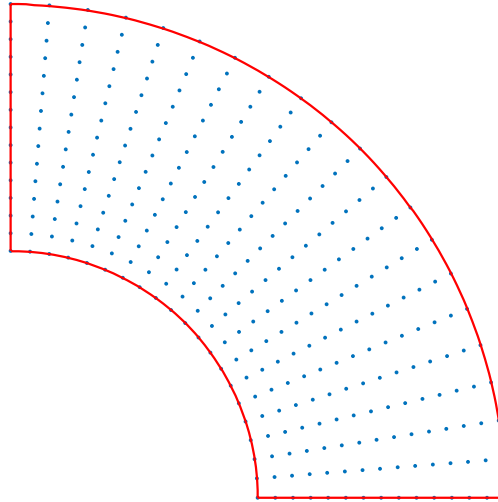
$$\sigma_\theta = \frac{b^2}{b^2 - a^2} \left(1 + \frac{a^2}{r^2} \right) p \quad (4.4)$$

$$\tau_{r\theta} = 0$$

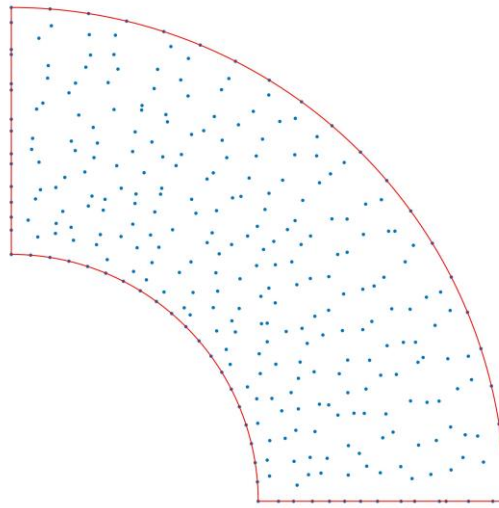
$$u_r = \frac{1}{E} \left(\frac{(1-\nu)b^2 p}{b^2 - a^2} r + \frac{(1+\nu)a^2 b^2}{b^2 - a^2} \frac{1}{r} \right) \quad (4.5)$$

$$u_\theta = 0$$

To study the convergence of the FPM for displacements and the strain energy, regularly distributed 15×11 , 15×16 and 15×21 points are considered (shown in Figure 12(a)). The relation between h , defined as the longest distance of two neighbouring Points, and relative errors are given in Figure 13, where R stands for the convergence rate.



(a)



(b)

Figure 12(a). The regular distribution of 15×21 points

(b). The irregular distribution of 15×21 points

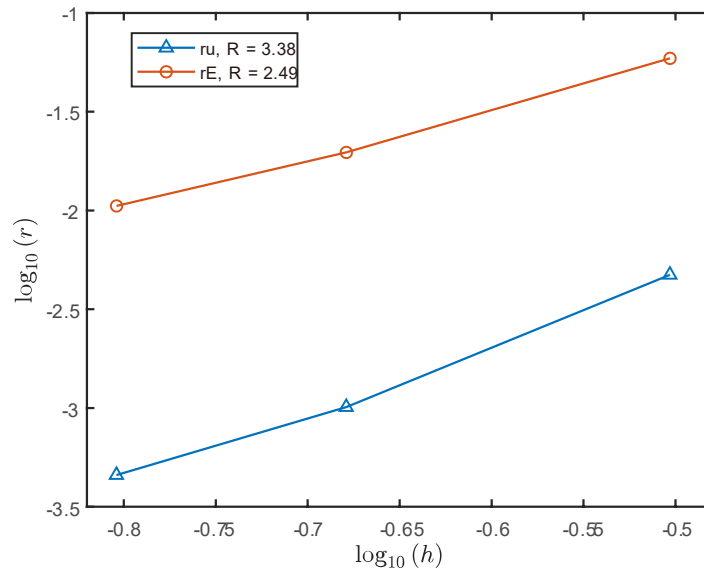
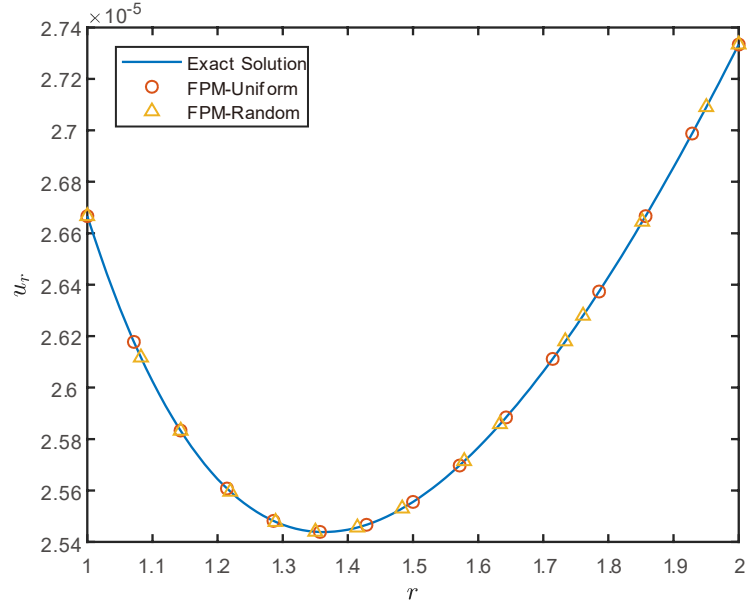
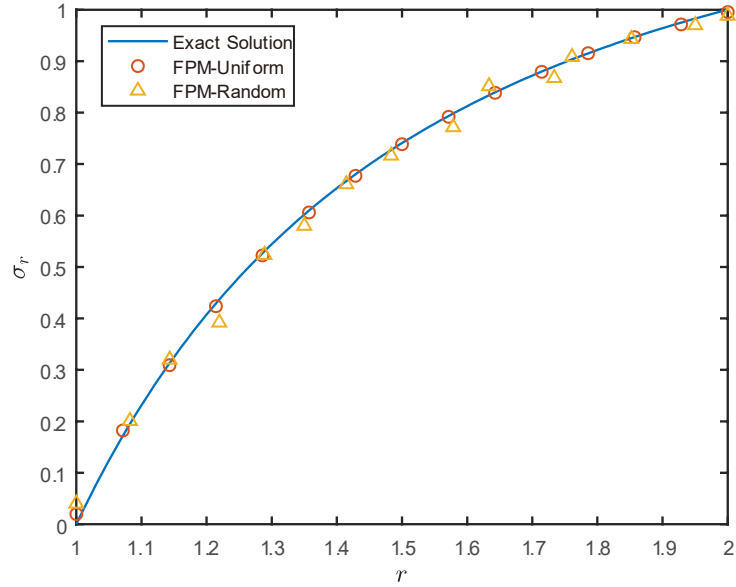


Figure 13. Relative errors and convergence rates for the problem

Additionally, numerical solutions of u_r and σ_r along $\theta = 0$ with 15×21 Points distributed regularly and randomly are shown in Figure 14(a) and (b), respectively. The irregular distribution of Points is illustrated in Figure 12(b). It can be seen that the FPM can solve the displacements and stresses with a satisfactory accuracy for both the situations.



(a)



(b)

Figure 14(a). Numerical solutions of u_r along $\theta = 0$

(b). Numerical solutions of σ_r along $\theta = 0$

4.4 Infinite plate with a circular hole

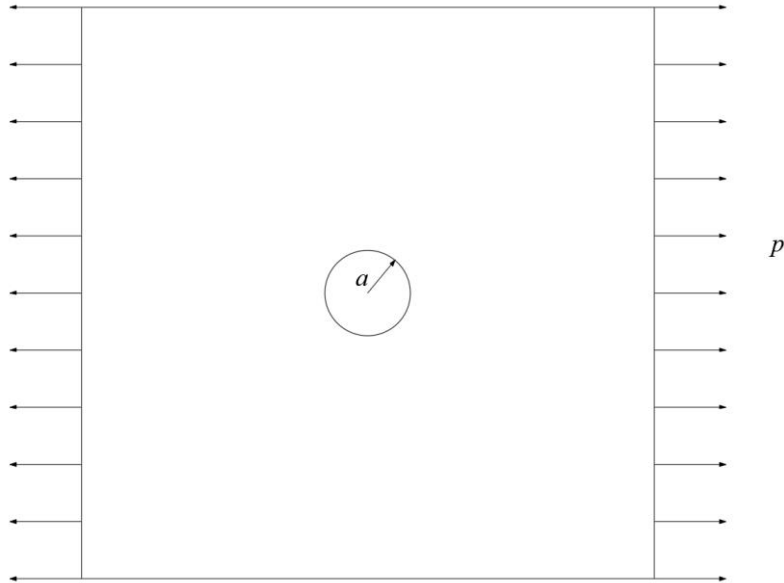
In this part, we employ the FPM to model an infinite plate with a circular hole. As shown in Figure 15(a), the circular hole (radius equals a) locates at the plate's center and a uniform tensile stress p is imposed in the x direction at infinity. The exact

solutions for stresses and displacements are given in Eqs. (4.6) and (4.7) respectively.

$$\begin{aligned}\sigma_x &= p \left[1 - \frac{a^2}{r^2} \left(\frac{3}{2} \cos 2\theta + \cos 4\theta \right) + \frac{3a^4}{2r^4} \cos 4\theta \right] \\ \tau_{xy} &= p \left[-\frac{a^2}{r^2} \left(\frac{1}{2} \sin 2\theta + \sin 4\theta \right) + \frac{3a^4}{2r^4} \sin 4\theta \right] \\ \sigma_y &= p \left[-\frac{a^2}{r^2} \left(\frac{1}{2} \cos 2\theta - \cos 4\theta \right) - \frac{3a^4}{2r^4} \cos 4\theta \right]\end{aligned}\quad (4.6)$$

$$\begin{aligned}u_x &= \frac{1+\nu}{E} p \left(\frac{1}{1+\nu} r \cos \theta + \frac{2}{1+\nu} \frac{a^2}{r} \cos \theta + \frac{1}{2} \frac{a^2}{r} \cos 3\theta - \frac{1}{2} \frac{a^4}{r^3} \cos 3\theta \right) \\ u_y &= \frac{1+\nu}{E} p \left(\frac{-\nu}{1+\nu} r \sin \theta - \frac{1-\nu}{1+\nu} \frac{a^2}{r} \sin \theta + \frac{1}{2} \frac{a^2}{r} \sin 3\theta - \frac{1}{2} \frac{a^4}{r^3} \sin 3\theta \right)\end{aligned}\quad (4.7)$$

Based on the symmetry of the problem, we simplify the model by considering a quarter of the plate, as shown in Figure 15(b). Symmetry boundary conditions $u_x = 0$, $t_y = 0$ at $x = 0$ and $u_y = 0$, $t_x = 0$ at $y = 0$, are imposed. Displacement boundary conditions are imposed on the upper side ($y = 2$) and right side ($x = 2$) according to Eq. (4.7). The edge at $r = 1$ is set to be a free boundary.



(a)

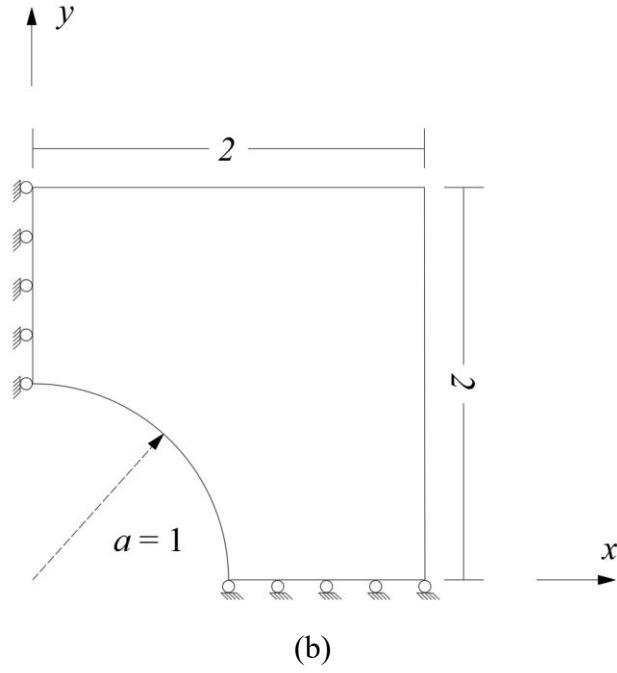


Figure 15 (a). An infinite plate with a circular hole under remote tension

(b). The simplified model after considering symmetry

The problem is solved considering plane stress with $E = 1$ and $\nu = 0.3$. The penalty coefficient η is set to be E . 805 Points are distributed randomly in the domain (shown in Figure 16).

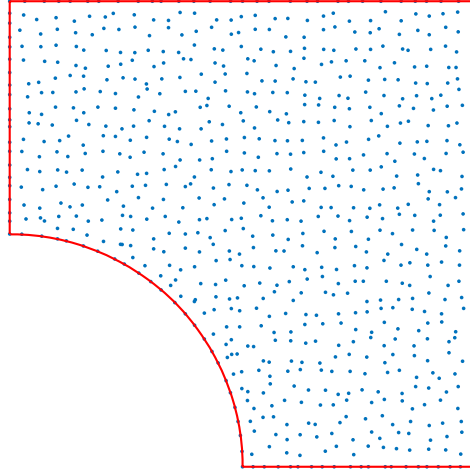
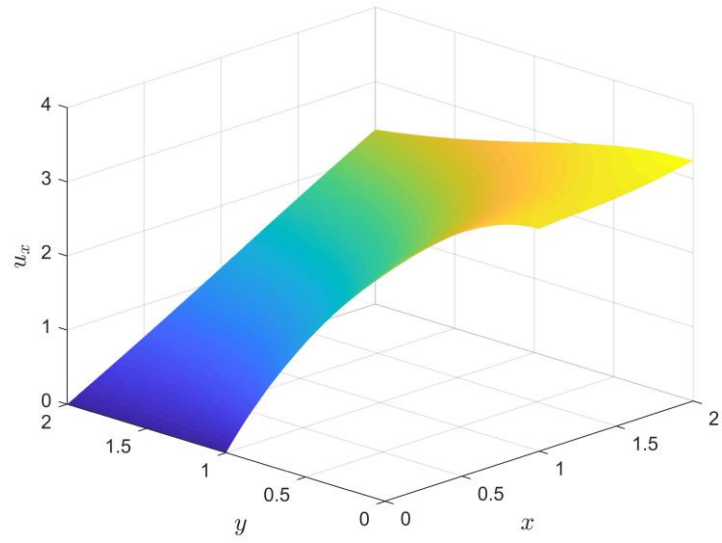
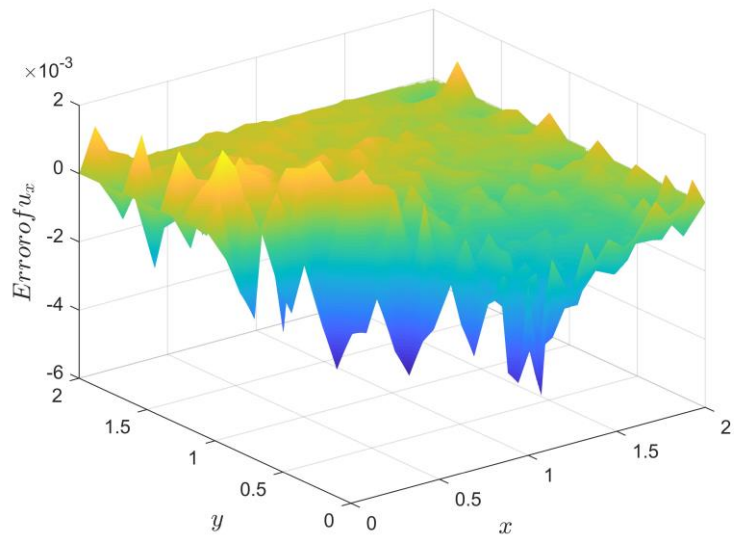


Figure 16. The Random distribution of Points

The numerical solution of u_x and the corresponding error compared to the exact solution are given in Figure 17(a) and (b), respectively. Relative errors are $r_u = 3.83 \times 10^{-4}$ and $r_E = 1.84 \times 10^{-2}$.



(a)

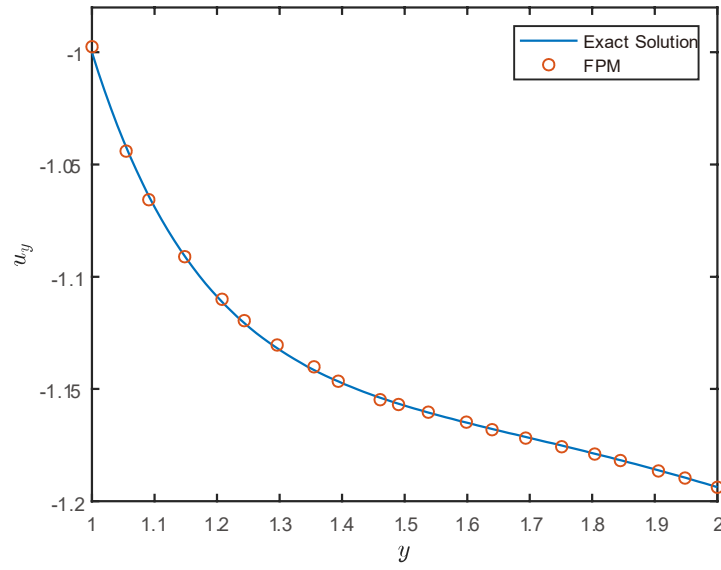


(b)

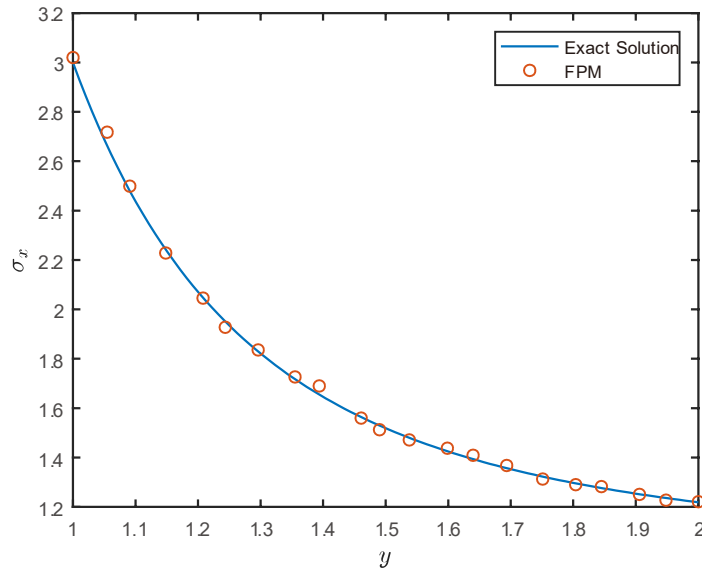
Figure 17(a). The numerical solution of u_x

(b). The error of u_x

Additionally, the numerical solutions of u_y and σ_x along $x = 0$, as compared to the exact solutions are present in Figure 18(a) and (b), respectively. We can see that the FPM gives satisfactory solutions to this stress concentration problem.



(a)



(b)

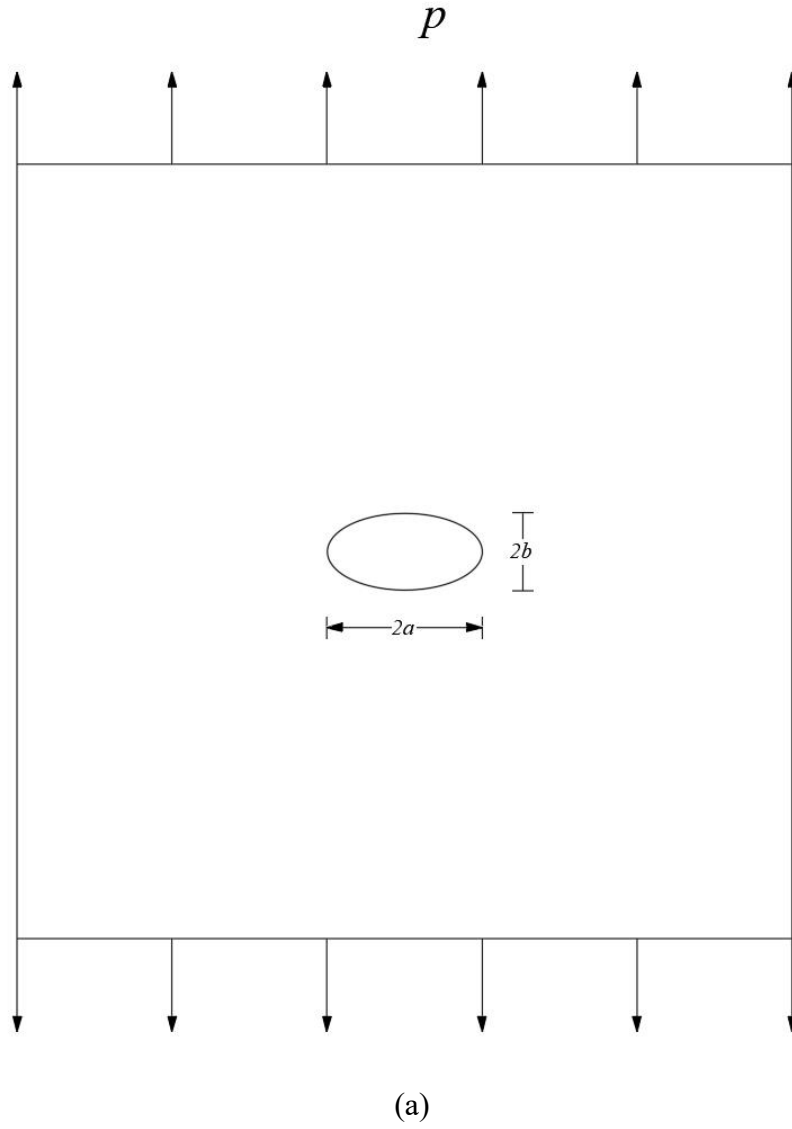
Figure 18(a). The numerical solution of u_y along $x = 0$

(b). The numerical solution of σ_x along $x = 0$

4.5 Infinite plate with an elliptic hole

An infinite plate with an elliptic hole at its center and subjected to a uniform tension in y direction is studied in this section (shown in Figure 19(a)). The tensile stress p is set as 1 in this study. A quarter of this plate is simulated, as shown in Figure 19(b), with the major axis $a = 2$ and the minor axis $b = 1$. Exact solutions of this problem are given

in [15]. Because of the symmetry of the model, boundary conditions $u_x = 0$, $t_y = 0$ and $u_y = 0$, $t_x = 0$ are prescribed on the left and bottom edges, respectively. Free boundary conditions are imposed on the elliptic edge. For the upper and right edges, displacement boundary conditions are imposed according to the exact solutions.



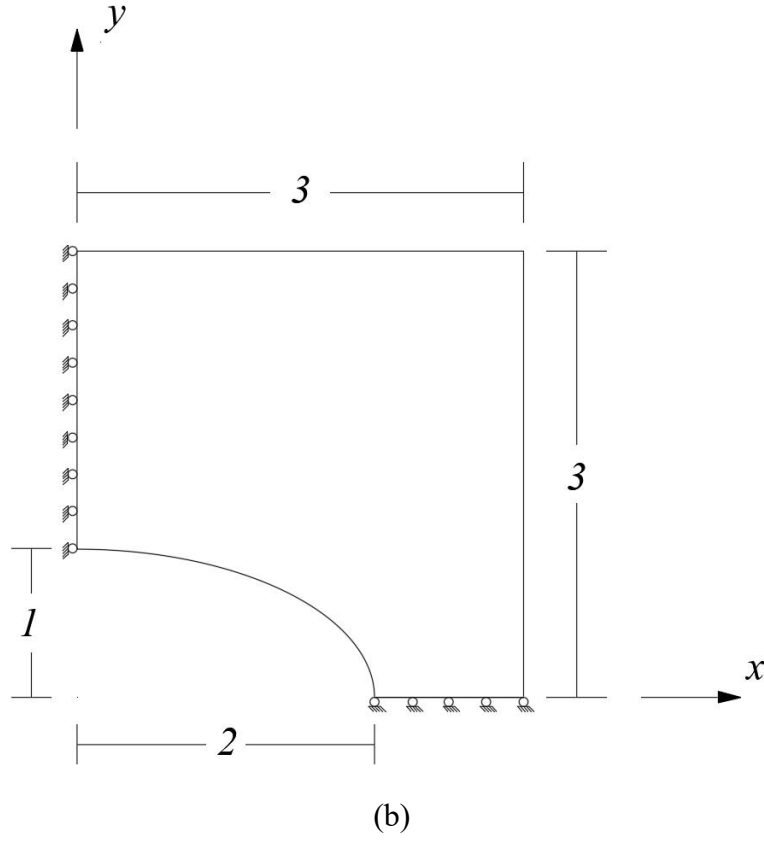


Figure 19(a). An infinite plate with an elliptic hole under remote tension

(b). The simplified model after considering symmetry

The irregular distribution of 825 Points is illustrated in Figure 20. This problem is solved considering plane stress with $E = 1$ and $\nu = 0.3$. The penalty coefficient η is equal to E . The relative errors of the numerical solution by the FPM are: $r_u = 1.74 \times 10^{-3}$ and $r_E = 3.69 \times 10^{-2}$. The numerical solutions of u_x and σ_y along $y = 0$ as compared to the exact solutions are present in Figure 21(a) and (b), respectively. We can see that the stress concentration phenomenon is simulated with satisfactory accuracy.

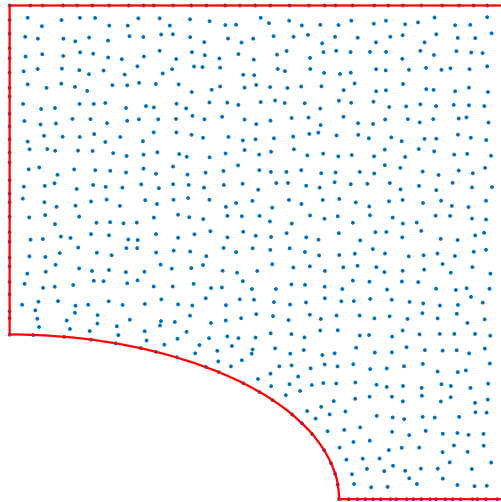
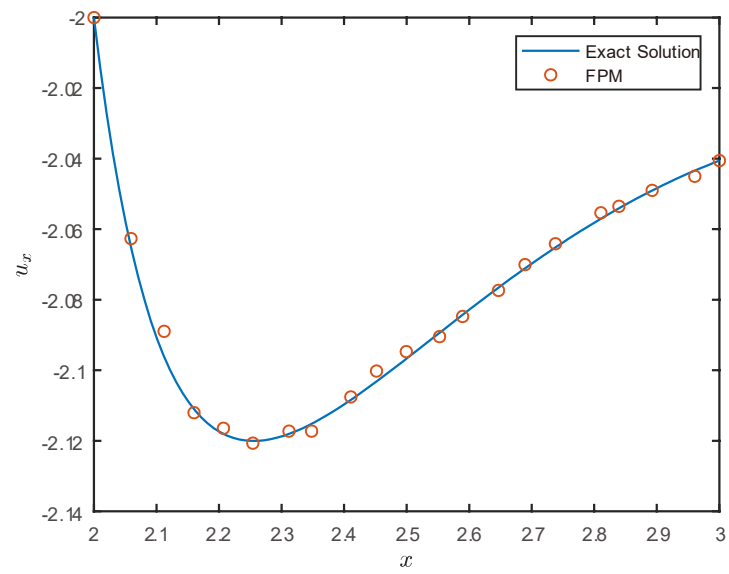
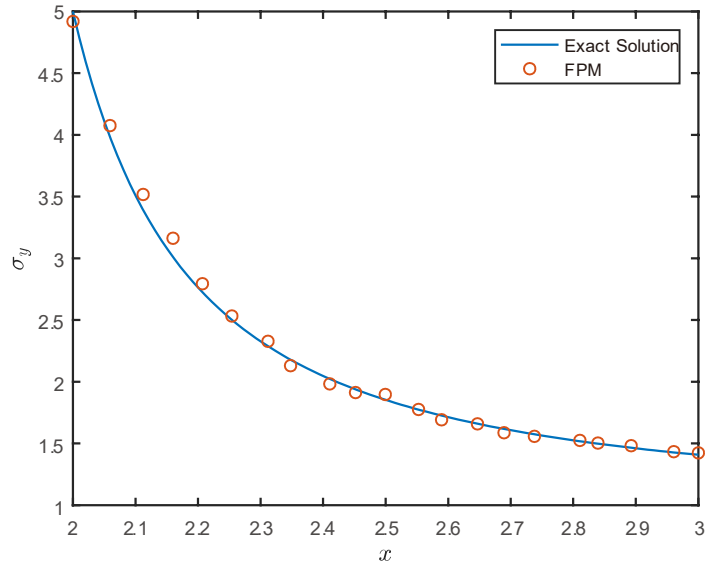


Figure 20. The irregular distribution of Points



(a)



(b)

Figure 21(a). The numerical solution of u_x along $y = 0$

(b). The numerical solution of σ_y at $y = 0$

4.6 Infinite plate with a pre-existing crack

In this section, we apply the FPM to model a pre-existing crack. Specifically, a mode-I crack problem is considered. The analytical displacement and stress fields near the crack tip for a mode-I crack are given in Eq. (4.8) and Eq. (4.9), respectively [16], where (r, θ) are polar coordinates measured from the crack tip and K_I is the mode-I stress intensity factor.

$$\begin{Bmatrix} u_x \\ u_y \end{Bmatrix} = \frac{K_I}{2\mu} \sqrt{\frac{r}{2\pi}} \begin{Bmatrix} \cos \frac{\theta}{2} \left[\kappa - 1 + 2 \sin^2 \frac{\theta}{2} \right] \\ \sin \frac{\theta}{2} \left[\kappa + 1 - 2 \cos^2 \frac{\theta}{2} \right] \end{Bmatrix} \quad (4.8)$$

$$\text{where } \kappa = \frac{3 - \bar{\nu}}{1 + \bar{\nu}} \quad \mu = \frac{\bar{E}}{2(1 + \bar{\nu})}$$

$$\begin{Bmatrix} \sigma_x \\ \sigma_y \\ \tau_{xy} \end{Bmatrix} = \frac{K_I}{\sqrt{2\pi r}} \cos \frac{\theta}{2} \begin{Bmatrix} 1 - \sin \frac{\theta}{2} \sin \frac{3\theta}{2} \\ 1 + \sin \frac{\theta}{2} \sin \frac{3\theta}{2} \\ \sin \frac{\theta}{2} \cos \frac{3\theta}{2} \end{Bmatrix} \quad (4.9)$$

As shown in Figure 22, a single edge-cracked square plate with width = b and crack length = a is studied. Displacement boundary conditions are imposed on its four sides according to Eq. (4.8) with K_I prescribed as 1. This problem is analyzed considering plane stress. We prescribe that $b = 2a = 10$, $E = 1$, $\nu = 0.3$. The penalty coefficient η is set to be equal to E .

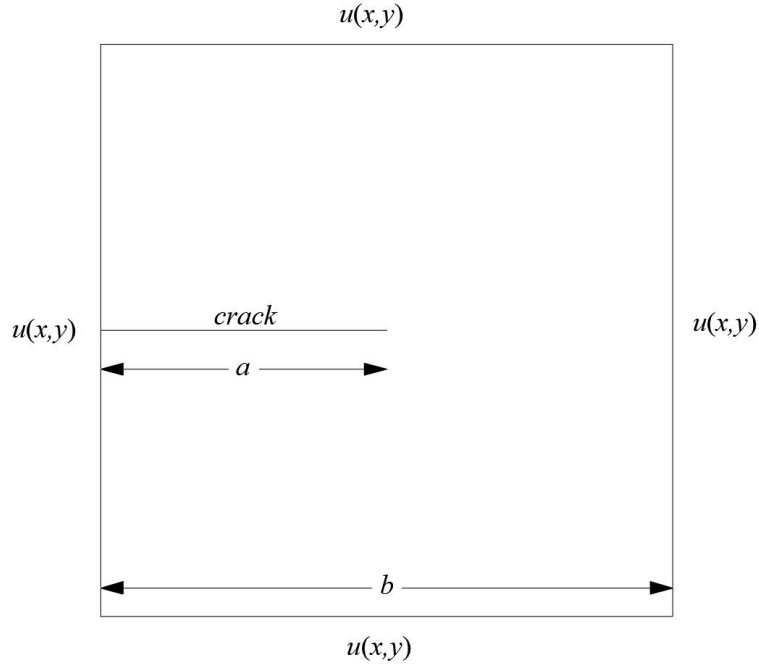


Figure 22. An edge-cracked square plate

40×40 Points are scattered regularly in the domain (shown in Figure 23). To simulate a pre-existing crack in the FPM, we define that all the boundaries that coincide with the crack are free boundaries. Besides, for those points located on one side of the crack, we prescribe that they will not be included in the supports of points located on the other side of the crack, in other words, they will not interact with each other when computing shape functions. For example, in Figure 24, we assume that a crack exists at boundaries Γ_{26} , Γ_{15} and Γ_{47} . Therefore, they are defined as free boundaries. The

support of Point 1 only contains Points 2,3,4 without Points 5 and the support of Point 5 does not include Point 1.

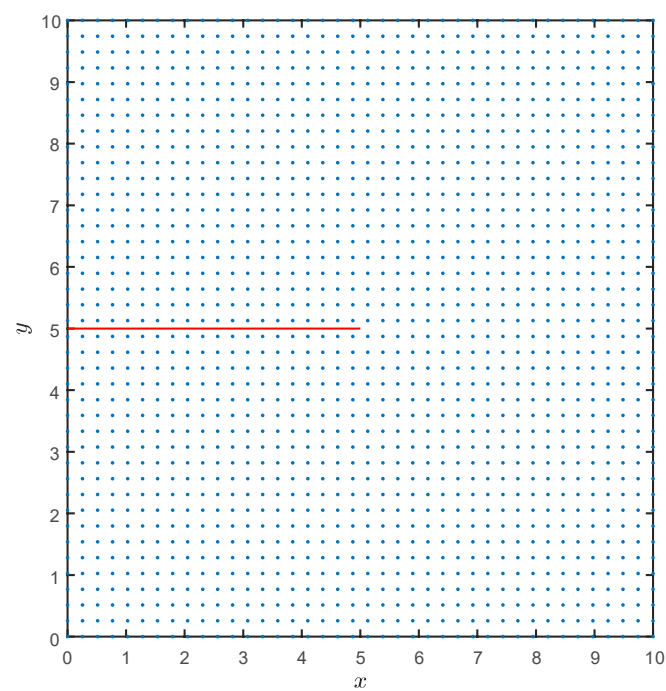


Figure 23. The regular distribution of Points

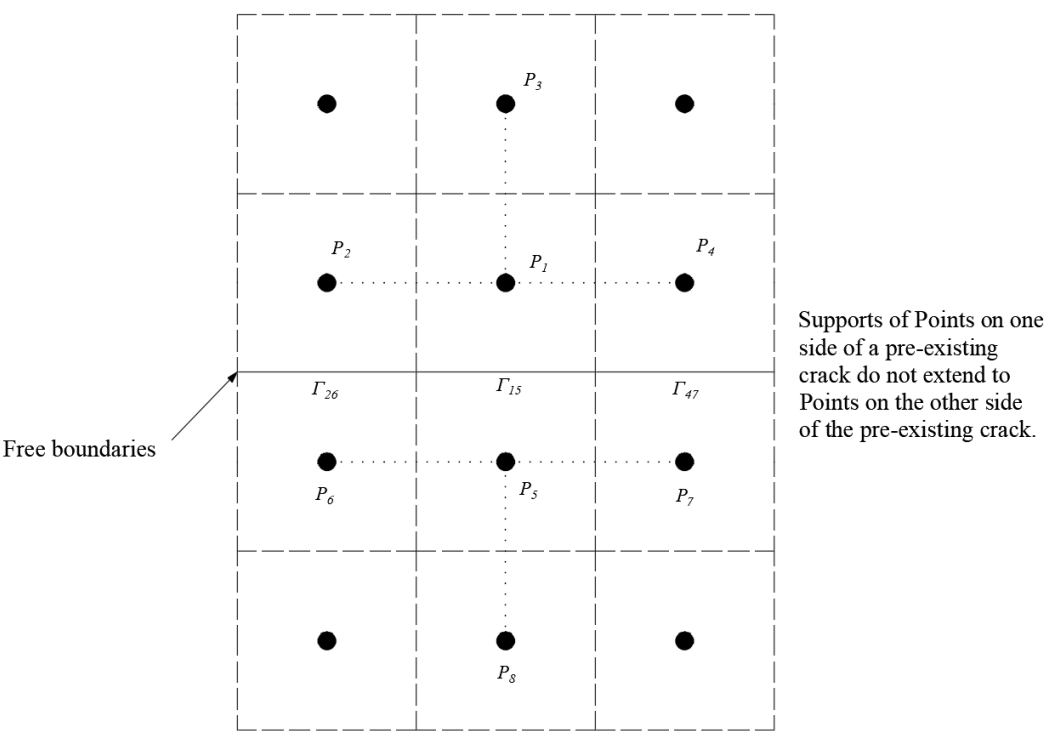
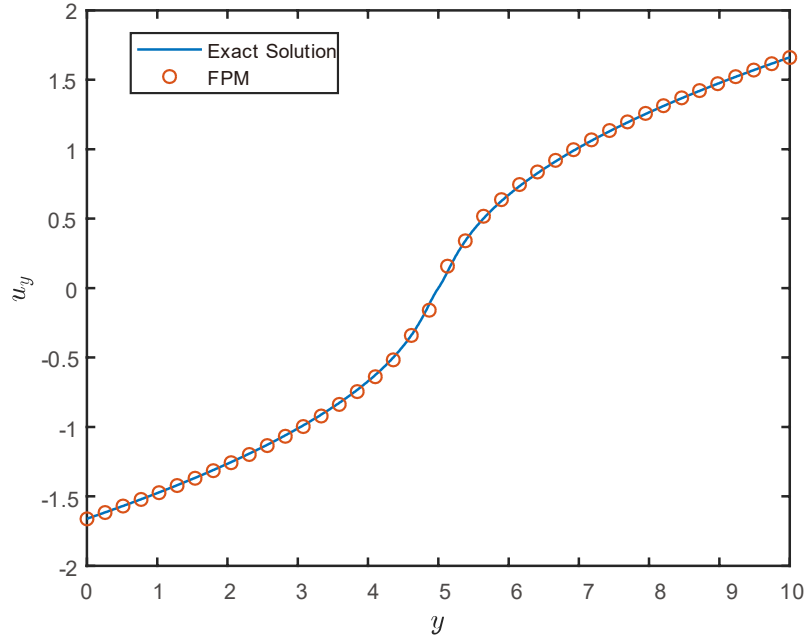
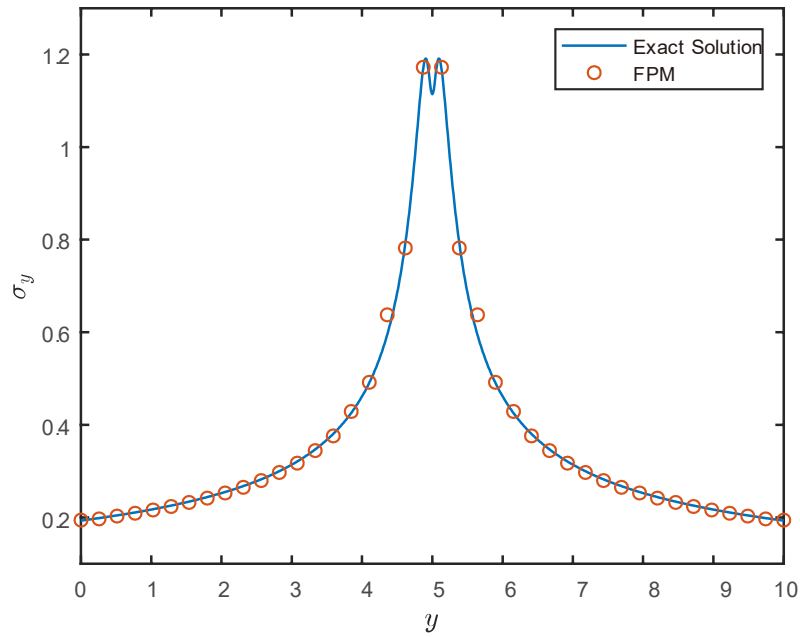


Figure 24. Free boundaries and supports of points

The numerical solutions of u_y and σ_y along $x = 5 + 0.5h$ (h is the distance between 2 neighboring Points) as compared to exact solutions are demonstrated in Figure 25(a) and (b), respectively. It can be seen that the numerical solutions obtained by the FPM can achieve excellent accuracy.



(a)



(b)

Figure 25(a). The numerical solution of u_y along $x = 5+0.5h$

(b). The numerical solution of σ_y along $x = 5+0.5h$

Besides, we further evaluate the mode-I stress intensity factor K_I by calculating the J -integral. The contour for the J -integral is shown in Figure 26 while $w = 2.5h$ and $l = 4.5h$. The solution of K_I by computing the J -integral is shown in Table I, which is very accurate as compared with the exact solution.

Table I. Stress intensity factor for the pre-existing edge crack problem

K_I (J -integral)	K_{exact}	Error
0.9917	1	0.0083

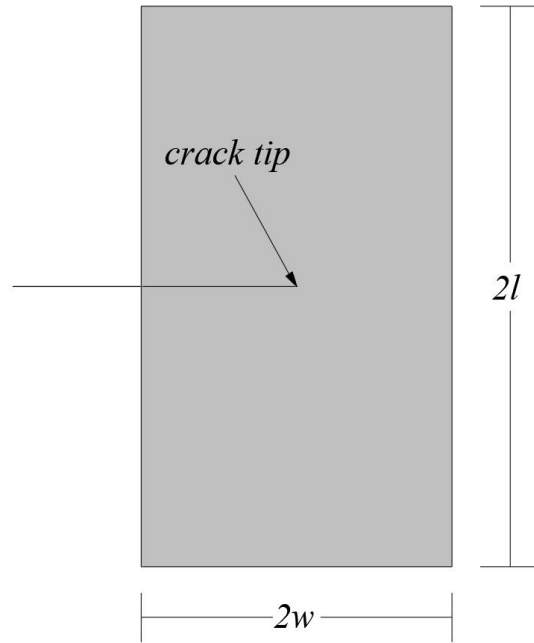


Figure 26. The contour for the J -integral

5. CONCLUSIONS

In this paper, we have employed the FPM to solve linear elasticity problems. Simple, Local, polynomial, discontinuous and Point-based trial and test functions are constructed in the FPM and Numerical Flux Corrections are introduced to surmount the inconsistency caused by the discontinuity. Eventually, in the FPM, based on the

Galerkin method, a sparse, symmetric and positive definitive global stiffness matrix can be derived by assembling all the local Point Stiffness Matrices. Since trial and test functions are polynomial, all integrals in the Galerkin weak form can be easily and exactly computed in the FPM. From the examples provided in Section 4, we demonstrate the convergence, robustness, consistency and high accuracy of the FPM in elasticity problems. Volume locking does not occur in the FPM for nearly incompressible materials and stress concentration phenomena are also simulated exactly.

Besides all these advantages we mentioned, the FPM also possesses the ability to model either pre-existing cracks or physically forming cracks, rupture and fragmentation exactly and easily. In the FEM, when we introduce a crack between two adjoining elements, we have to divide them into unconnected elements. Adding new points is usually inevitable for this remeshing work [17]. Since the number of DOFs changes and the connectivity of elements is modified in each calculation step, the dimensions of the global stiffness matrix and the load vector varies constantly. We can see that simulating cracks which either form physically or propagate is such a complex task for the FEM. However, due to the discontinuity of the FPM, it will cost less effort to model a crack between two adjoining subdomains. If a crack emerges at an internal boundary or rupture forms physically, we only need to redefine it as a free boundary and change relevant shape functions. According to Eq. (3.8), we only need to delete three boundary integrals about it on the left side while the right side stays the same. Just a slight modification of the global stiffness matrix can complete this operation without adding new Points.

From the above analysis, we can conclude that the FPM is an accurate, robust and consistent meshless Galerkin weak-form method with less computational cost. It also possesses great potential to solve extreme problems of rupture, and fragmentation. The simulation of crack propagation and the phenomena of rupture and fragmentation by the FPM will be discussed in our forthcoming paper.

ACKNOWLEDGEMENTS

The first two authors thankfully acknowledge the support from the National Key Research and Development Program of China (No. 2017YFA0207800).

REFERENCES

1. OC Zienkiewicz, RL Taylor, JZ Zhu. The Finite Element Method: Its Basis and Fundamentals (Seventh Edition). 2005.
2. T Belytschko, YY Lu, L Gu. Element-free Galerkin methods. *International journal for numerical methods in engineering* 1994; 37(2):229-256.
3. SN Atluri, T Zhu. A new meshless local Petrov–Galerkin (MLPG) approach. *Computational Mechanics* 1998; 22(2):117-127.
4. T Belytschko, M Tabbara. Dynamic fracture using element-free Galerkin methods. *International Journal for Numerical Methods in Engineering* 1996; 39(6):923-938.
5. Z Han, A Rajendran, S Atluri. Meshless local Petrov-Galerkin (MLPG) approaches for solving nonlinear problems with large deformations and rotations. *Computer Modeling in Engineering and Sciences* 2005; 10(1):1.
6. M Hillman, JS Chen. An accelerated, convergent, and stable nodal integration in Galerkin meshfree methods for linear and nonlinear mechanics. *International Journal for Numerical Methods in Engineering* 2016; 107(7):603-630.
7. LB Lucy. A numerical approach to the testing of the fission hypothesis. *Astronomical Journal* 1977; 82(82):1013-1024.
8. SA Silling, F Bobaru. Peridynamic modeling of membranes and fibers. *International Journal of Non-Linear Mechanics* 2005; 40(2):395-409.
9. L Dong, T Yang, K Wang, SN Atluri. A new Fragile Points Method (FPM) in computational mechanics, based on the concepts of Point Stiffnesses and Numerical Flux Corrections. In: *arXiv e-prints*; 2019.
10. T Liszka, J Orkisz. The finite difference method at arbitrary irregular grids and its application in applied mechanics. *Computers & Structures* 1980; 11(1):83-95.
11. DN Arnold, F Brezzi, B Cockburn, LD Marini. Unified Analysis of Discontinuous Galerkin Methods for Elliptic Problems. *Siam Journal on Numerical Analysis* 2002; 39(5):1749-1779.

12. B Riviere. Discontinuous Galerkin Methods For Solving Elliptic And Parabolic Equations: Theory and Implementation. 2008; 35.
13. Z Han, S Atluri. On the (meshless local petrov-galerkin) mlpg-eshelby method in computational finite deformation solid mechanics-part ii. *CMES: Computer Modeling in Engineering & Sciences* 2014; 97(3):199-237.
14. SN Atluri, TL Zhu. The meshless local Petrov-Galerkin (MLPG) approach for solving problems in elasto-statics. *Computational Mechanics* 2000; 25(2-3):169-179.
15. NI Muskhelishvili. Some basic problems of the mathematical theory of elasticity. Springer Science & Business Media; 2013.
16. TL Anderson. Fracture mechanics: fundamentals and applications. CRC press; 2017.
17. GT Camacho, M Ortiz. Computational modelling of impact damage in brittle materials. *International Journal of Solids and Structures* 1996; 33(20):2899-2938.